

High-Performance Moment-Encoded Lattice Boltzmann Method with Stability-Guided Quantization

YIXIN CHEN, University of Toronto, Canada

WEI LI*, Shanghai Jiao Tong University, China

DAVID I.W. LEVIN, University of Toronto, Canada and Nvidia, Canada

KUI WU, Lightspeed, USA

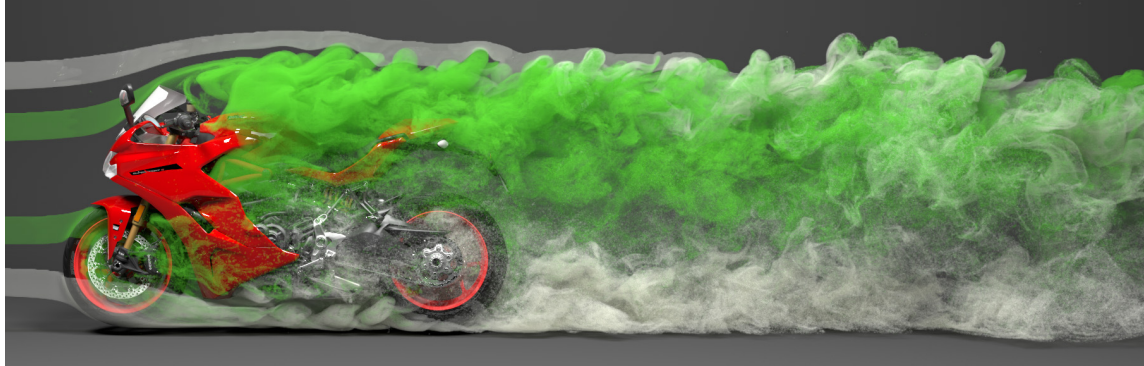


Fig. 1. Large-scale turbulent flow interacting with complex geometry. Snapshot of a turbulent smoke simulation around a Ducati motorcycle on a $1000 \times 400 \times 400$ grid using our GPU-optimized LBM solver with 16-bit quantization. The simulation preserves rich, fine-scale vortical structures and remains numerically stable under highly intricate boundary conditions. Compared to HOME-LBM [Li et al. 2023], our method reduces the memory footprint by 25% and achieves 4.3 \times speedup, enabling practical high-resolution, large-scale flow simulation on a single GPU.

In this work, we present a memory-efficient, high-performance GPU framework for moment-based lattice Boltzmann methods (LBM) with fluid–solid coupling. We introduce a split-kernel scheme that decouples fluid updates from solid boundary handling, substantially reducing warp divergence and improving utilization on GPUs. We further perform the first von Neumann stability analysis of the high-order moment-encoded LBM (HOME-LBM) formulation, characterizing its spectral behavior and deriving stability bounds for individual moment components. These theoretical insights directly guide a practical 16-bit moment quantization without compromising numerical stability. Our framework achieves up to 6 \times speedup and reduces GPU memory footprint by up to 50% in fluid-only scenarios and 25% in scenes with complex solid boundaries compared to the state-of-the-art LBM solver, while preserving physical fidelity across a range of large-scale benchmarks and real-time demonstrations. The proposed approach enables scalable, stable, and high-resolution LBM simulation on a single GPU, bridging theoretical stability analysis with practical GPU algorithm design.

CCS Concepts: • Computing methodologies → Physical simulation.

Additional Key Words and Phrases: fluid simulation; lattice Boltzmann method; GPU computing; quantization; fluid-solid coupling



Fig. 2. 3D Smoke over an F1 Car. Smoke around an F1 car highlights a complex, multi-scale wake: strong shear layers from the wheels, rear wing, and diffuser roll up into coherent vortices near the vehicle, then stretch and break down into a turbulent, filamentary plume downstream.

1 Introduction

Fluid simulation plays a central role in computer graphics, enabling realistic simulation of natural phenomena such as wind, smoke, and fire. Beyond visual fidelity, high-performance fluid simulation has become increasingly critical for downstream applications, including shape design [Ma et al. 2021], robotic control in virtual environments [Hu et al. 2025; Liu et al. 2022a; Ma et al. 2018; Song et al. 2025; Xian et al. 2023], and inverse optimization problems [Chen et al. 2024; Du et al. 2020; Li et al. 2022a].

Stable fluids [Stam 1999], which solves the Navier–Stokes (NS) equations on Eulerian grids, was proposed decades ago and remains widely used in real-time applications due to its simplicity, efficiency, and stability.

While subsequent research has sought to accelerate computation and preserve fine-scale details, it remains challenging in practice to achieve stable, high-resolution simulations under tight real-time constraints. Grid-based solvers typically rely on global pressure solves and incur nontrivial synchronization and communication overhead across the grid. Particle-based solvers, in contrast, are often dominated by expensive neighbor searches, irregular memory access, and dynamic data structures, leading to poor throughput and utilization on GPUs. Together, these bottlenecks limit their scalability on modern GPUs and become increasingly costly as resolution and geometric complexity grow.

In contrast to macroscopic solvers, the lattice Boltzmann method (LBM) has emerged as a compelling alternative for simulating turbulent weakly compressible flows, favored for its massive parallelism and superior vortex-preserving properties. Operating locally on discretized nodes at the mesoscopic scale, LBM is inherently well-suited for GPU acceleration. However, standard LBM schemes impose a heavy memory burden: each node in a D3Q27 lattice structure requires storing two sets of 27 floating-point distribution functions, resulting in severe memory traffic and limited scalability. To address this limitation, Li et al. [2023] propose the High-Order Moment-Encoded LBM (HOME-LBM), which reduces memory consumption by storing a compact set of velocity moments instead of the full lattice distribution functions. In addition, a more lightweight collision operator is applied directly in moment space. This formulation substantially reduces memory footprint and bandwidth demand, and has been shown to improve numerical robustness in turbulent flow simulations. However, its moment-based solid coupling relies on costly link–solid intersection tests and highly divergent branching, leading to poor GPU utilization. In addition, the method still requires double buffering for

*Corresponding author.

Authors' Contact Information: **Yixin Chen**, yixin.chen@mail.utoronto.ca, University of Toronto, Toronto, Canada; **Wei Li**, 1104720604wei@gmail.com, Shanghai Jiao Tong University, Shanghai, China; **David I.W. Levin**, University of Toronto, Toronto, ON, Canada and Nvidia, Toronto, ON, Canada, diwlevin@cs.utoronto.edu; **Kui Wu**, walker.kui.wu@gmail.com, Lightspeed, Los Angeles, USA.

ping-pong updates, thereby limiting the maximum simulation domain size under fixed GPU memory budgets. Although quantization has proven effective for reducing memory footprint and bandwidth in large-scale simulations [Hu et al. 2021; Liu et al. 2022b], it remains unclear how to design a stable quantization scheme for LBM. As a result, achieving high computational efficiency, low memory footprint, and strong physical fidelity simultaneously remains challenging.

In this work, we present a high-performance, memory-efficient GPU approach for moment-based LBM. We introduce a decoupled fluid–solid coupling scheme that separates fluid advancement from solid interactions, significantly reducing GPU thread divergence. To further reduce memory usage, we, to our knowledge, perform the first von Neumann stability analysis tailored to HOME-LBM formulations, thereby deriving theoretical stability bounds for individual moments. These bounds directly guide a 16-bit quantization strategy that compresses moment data while preserving numerical stability. We validate our approach through real-time examples and comprehensive benchmarks against D3Q19 and D3Q27 configurations. We perform additional 2D numerical experiments for stability verification of the proposed quantized scheme. Overall, our framework achieves up to 6 \times speedup and substantial memory savings compared with state-of-the-art macroscopic and kinetic methods, while enabling efficient coupling with complex geometries and maintaining high visual quality and numerical stability in challenging turbulent scenarios.

2 Related Work

This section reviews prior work on numerical solvers for fluid simulation and their GPU acceleration strategies, von Neumann stability analysis for LBM, and recent advances in quantization and data compression in graphics.

Navier-Stokes solvers. Macroscopic Navier-Stokes solvers have long been the backbone of graphics fluid simulation. As a seminal work, Stam [1999] introduces stable fluids to solve the Navier–Stokes (NS) equations on Eulerian grids using an unconditionally stable semi-Lagrangian advection scheme. This approach enabled fluid simulations with larger time steps, significantly improving efficiency for computer graphics applications, but suffers from excessive numerical diffusion. To mitigate this issue, a variety of improved advection schemes have been proposed, including BFECC [Kim et al. 2005], the modified MacCormack scheme [Selle et al. 2008], MacCormack with reflection (MC+R) [Zehnder et al. 2018], bidirectional flow maps [Qu et al. 2019], covector advection [Nabizadeh et al. 2022], neural flow maps [Deng et al. 2023], the Eulerian vortex method on flow maps [Wang et al. 2024] and leapfrog flow maps [Sun et al. 2025], all of which aim to better preserve vortical details over time.

Beyond Eulerian methods, Lagrangian particle-based approaches, such as smoothed particle hydrodynamics (SPH) [Akinci et al. 2012; Peer et al. 2015; Solenthaler and Pajarola 2009], have also been explored; however, these methods struggle to capture turbulence at low particle counts. Hybrid Eulerian–Lagrangian approaches, such as FLIP-based extensions [Fu et al. 2017; Jiang et al. 2015; Nabizadeh et al. 2024; Zhang et al. 2016], improve accuracy by combining grid and particle representations. Vortical structures can be preserved more effectively with vortex methods, including vortex particles [Selle et al. 2005], vortex filaments [Weismann and Pinkall 2010], and vortex sheets [Pfaff et al. 2012; Zhang et al. 2015], which provide scalable strategies for maintaining fine-scale flow details.

The computational power of modern GPUs has enabled substantial acceleration of fluid solvers through multigrid methods [Chentanez and Müller 2011; Sun et al. 2025], fixed-point iterations [Chen et al. 2015], and compact Poisson filters [Rabbani et al. 2022], as well as multi-GPU parallelization for large-scale simulations [Horvath and Geiger 2009; Wang et al. 2020]. Despite these advances, hybrid Eulerian–Lagrangian approaches [Gao et al. 2018], while offering improved fidelity and accuracy, still lead to significant memory overhead due to the need to maintain both grids and

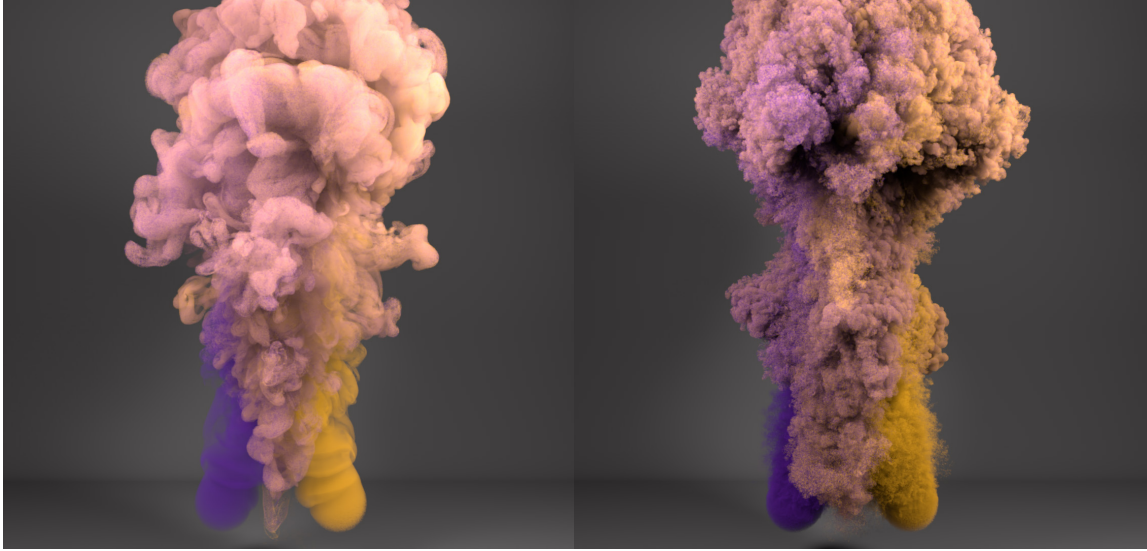


Fig. 3. 3D High-Resolution Plume. Fluid-only plume simulation using 16-bit quantized kinetic solver at a grid resolution of 1024^3 . Left: Reynolds number $Re = 40,960$. Right: Reynolds number $Re = 2,048,000$.

particles. Moreover, grid-based Poisson solvers typically rely on iterative methods that require numerous GPU kernel launches, which limits overall performance.

Boltzmann-based solvers. The lattice Boltzmann method (LBM), a mesoscopic numerical approach, has recently emerged as a compelling alternative to traditional incompressible NS solvers for both single-phase [Li et al. 2020, 2023; Lyu et al. 2021] and multiphase [Li and Desbrun 2023; Li et al. 2021, 2022b; Wang et al. 2025] flows. Early graphics applications [Li et al. 2003; Thürey and Rüde 2009] primarily rely on the low-order Bhatnagar–Gross–Krook (BGK) collision model [Chen and Doolen 1998], motivating the development of higher-order collision schemes such as central-moment multiple-relaxation-time (CM-MRT) models [Li et al. 2020], which reduce both dispersion and dissipation errors. Coupling fluids with solids in the LBM framework has also been extensively investigated, with approaches including the immersed boundary (IB) method [Li et al. 2020; Peskin 1972], a variety of bounce-back schemes [Ladd 1994; Liu and Liu 2023; Lyu et al. 2023, 2021], and hybrid macroscopic–mesoscopic boundary models [Liu et al. 2025], enabling applications such as underwater swimming and UAV training [Hu et al. 2025; Liu et al. 2022a; Song et al. 2025]. Since LBM operates locally at the mesoscopic scale on lattice nodes, it is highly suitable for GPU acceleration and large-scale simulations [Rinaldi et al. 2012]. Prior works [Chen et al. 2022; Lehmann 2022] improve parallel efficiency through cache-friendly data layouts and optimized immersed boundary (IB) implementations with separate domain-boundary treatments, which improve load balancing and reduce warp divergence. To further reduce memory overhead, Li et al. [2023] introduces HOME-LBM, which compresses per-node storage to 10 moment variables and reconstructs 27 distribution functions on the fly. However, HOME-LBM still requires expensive link-solid intersection tests and exhibits divergent branching during solid coupling, thereby reducing parallel efficiency and scalability.

Von Neumann stability analysis of LBM. Von Neumann (VN) stability analysis [Von Neumann and Richtmyer 1950] has been widely used to characterize numerical stability, dispersion, and dissipation in LBM. Early studies apply it to the BGK model [Sterling and Chen 1996] and demonstrate the superior stability of the MRT model [Lallemand and Luo



Fig. 4. 3D Hilbert Space-Filling Curve. Visualization of four different Hilbert curve levels mapped onto a volumetric domain with a grid resolution of $256 \times 512 \times 256$. From left to right, the images correspond to increasing curve refinement levels, illustrating progressively finer spatial traversal patterns within the volume.

2000]. Subsequent work further analyzed high-order and regularized schemes [Coreixas et al. 2017; Malaspina 2015; Siebert et al. 2008], as well as cascaded and central-moment MRT schemes [Chávez-Modena et al. 2018; Dubois et al. 2015; Geier et al. 2006]. While VN stability analysis has been widely used in LBM, a corresponding VN analysis for moment-encoded formulations remains largely unexplored.

Quantization in graphics. Data quantization provides a complementary strategy for reducing bandwidth. In graphics, custom number formats and automatic bit-width search have been explored [Hu et al. 2021; Liu et al. 2022b], but these approaches often rely on heuristic optimization or learning-based search, which are computationally intractable for the chaotic dynamics of turbulent LBM flows. Neural compression methods such as NeuralVDB [Kim et al. 2024] and ACORN [Martel et al. 2021] achieve impressive compression ratios but incur significant inference overhead, hindering high-frequency real-time updates. In contrast, we derive a stability-guided quantization strategy tailored to moment-encoded LBM, enabling aggressive compression with minimal runtime overhead and numerical robustness.

3 Background

Before introducing our stability-guided GPU optimization approach, we briefly review the fundamentals of the lattice Boltzmann method (LBM) and high-order moment-encoded formulations along with an analysis of the primary computational bottleneck. Together, these components form the algorithmic foundation of our proposed method.

3.1 Lattice Boltzmann Method (LBM)

In the context of single-phase fluid dynamics, the governing kinetic equation for the evolution of the particle distribution function is the Boltzmann equation [Shan et al. 2006]:

$$\frac{\partial f}{\partial t} + \mathbf{v} \cdot \nabla f = \Omega(f) + \mathbf{F} \cdot \nabla_{\mathbf{v}} f, \quad (1)$$

where $f(\mathbf{x}, \mathbf{v}, t)$ denotes the distribution function, \mathbf{F} represents external forces, and Ω is the collision operator that relaxes f towards the local thermodynamic equilibrium f^{eq} [Coreixas et al. 2017]. By discretizing time t into uniform timesteps, space \mathbf{x} into a regular lattice grid, and velocity \mathbf{v} into a finite set of q discrete directions, the continuous Boltzmann equation Eq. 1 turns to the lattice Boltzmann equation (LBE) in dimensionless units:

$$f_i(\mathbf{x} + \mathbf{c}_i, t + 1) - f_i(\mathbf{x}, t) = \Omega_i + F_i, \quad (2)$$

where $f_i(\mathbf{x}, t)$ is the distribution along the i -th lattice direction, \mathbf{c}_i is the corresponding lattice velocity vector, Ω_i is the discrete collision term, and F_i accounts for the effect of external forces projected onto distribution space. Note that in LBM dimensionless space $\Delta x = \Delta t = 1$. The evolution in Eq. 2 can be solved using an operator splitting strategy consisting of two steps: first, the distribution values are advected via streaming by computing:

$$f_i^*(\mathbf{x}, t) = f_i(\mathbf{x} - \mathbf{c}_i, t), \quad (3)$$

followed by a collision step expressed as:

$$f_i(\mathbf{x}, t + 1) = f_i^*(\mathbf{x}, t) + \Omega_i + F_i. \quad (4)$$

The macroscopic quantities, such as density ρ , linear momentum $\rho\mathbf{u}$, and the second-order momentum tensor $\rho\mathbf{S}$, can be recovered from the distribution as:

$$\rho = \sum_{i=0}^{q-1} f_i, \quad \rho\mathbf{u} = \sum_{i=0}^{q-1} \mathbf{c}_i f_i + \frac{1}{2} \mathbf{F}, \quad \rho\mathbf{S}_{\alpha\beta} = \sum_{i=0}^{q-1} (\mathbf{c}_{i\alpha} \mathbf{c}_{i\beta} - c_s^2 \delta_{\alpha\beta}) f_i, \quad (5)$$

where c_s is the lattice sound speed, and the greek indices α and β refer to tensor coordinates, i.e., $\mathbf{S} = \{S_{\alpha\beta}\}_{\alpha,\beta}$ for $\alpha, \beta \in \{x,y\}$ in 2D and $\{x,y,z\}$ in 3D.

3.2 High-Order Moment-Encoded LBM (HOME-LBM)

To reduce the memory footprint and bandwidth cost of standard LBM while preserving physical accuracy, Li et al. [2023] proposed the High-Order Moment-Encoded LBM (HOME-LBM). The key idea of HOME-LBM is to store velocity moments ρ , $\rho\mathbf{u}$, and $\rho\mathbf{S}$ in memory and reconstruct distribution functions on-the-fly using a third-order Hermite basis to offer a good balance between accuracy and computational efficiency.

High-order distribution reconstruction. Given density ρ , momentum $\rho\mathbf{u}$, and the second-order stress tensor $\rho\mathbf{S}$, distribution functions f can be reconstructed via the closed-form function $h(\rho, \mathbf{u}, \mathbf{S})$ as:

$$f_i = h_i(\rho, \mathbf{u}, \mathbf{S}) \quad (6)$$

$$= \rho w_i \left[1 + \frac{\mathbf{c}_i \cdot \mathbf{u}}{c_s^2} + \frac{\mathbf{H}^{[2]}(\mathbf{c}_i) : \mathbf{S}}{2c_s^4} + \sum_{\alpha\beta\gamma} \frac{H_{\alpha\beta\gamma}^{[3]}(\mathbf{c}_i) T_{\alpha\beta\gamma}}{2c_s^6} \right], \quad (7)$$

where

$$T_{\alpha\beta\gamma} = S_{\alpha\beta} u_\gamma + S_{\alpha\gamma} u_\beta + S_{\beta\gamma} u_\alpha - 2u_\alpha u_\beta u_\gamma.$$

Here c_s is the lattice sound speed ($c_s^2 = \frac{1}{3}$), w_i are the lattice weights associated with \mathbf{c}_i , and H denotes the Hermite polynomial basis, $\alpha\beta\gamma \in \{xxy, xyx, xxz, xzz, yzz, yyx, xyz\}$ are Cartesian indices [Wang et al. 2025].

Collision and streaming. After streaming, three post-streaming temporary moments ρ^* , $\rho^*\mathbf{u}^*$, and $\rho^*\mathbf{S}^*$ are recovered from the distribution functions based on Eq. 5. A high-order collision operator is then applied directly in moment space to update the density, velocity, and stress tensor. For completeness, the full update equations of the moment-space collision operator are provided in Appendix A.

Solid coupling. HOME-LBM performs fluid–solid coupling by reconstructing boundary distribution functions at solid intersection points and replacing the corresponding streamed distributions on lattice links. Specifically, when a lattice

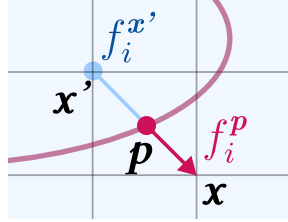


Fig. 5. Solid boundary intersection. Illustration of fluid lattice nodes intersecting with a solid surface.

link originating from a grid node x intersects a solid boundary at point p , a boundary distribution is reconstructed at p and streamed back to the grid node.

Under the assumption of a homogeneous weakly-compressible fluid, $\rho^p = \rho^x$. Velocity u^p can be computed based on the linear velocity and angular velocity of the solid at p . The rank-2 tensor S^p is approximated as:

$$S_{\alpha\beta}^{p,\text{eq}} = u_\alpha^p u_\beta^p, \quad S_{\alpha\beta}^p = u_\alpha^p u_\beta^p + (S_{\alpha\beta}^x - u_\alpha^x u_\beta^x). \quad (8)$$

Given velocity moments at p , f_i^p is reconstructed using Eq. 6 and stream it to x . Finally, the impact of the fluid on a solid is evaluated by summing all the contributions of all nodes x whose links intersect the solid with force and torque.

4 GPU-Oriented Redesign of HOME-LBM

4.1 GPU Bottlenecks in HOME-LBM

HOME-LBM [Li et al. 2023] achieves notable speedup over prior GPU-based LBM implementations [Li et al. 2020] through several key design choices. First, it reduces the per-node storage from 27 distribution functions to 10 moment variables, significantly lowering memory footprint and bandwidth demand. Second, by reconstructing distribution functions on the fly from stored moments, the streaming step can be executed more efficiently within the same block using shared memory. Moreover, collision, streaming, and solid coupling are fused into a single GPU kernel, eliminating multi-kernel launch overhead and improving overall throughput.

However, when complex solid geometries are present, solid coupling becomes the dominant computational bottleneck. For high-resolution triangle meshes, the per-step runtime can increase substantially compared to fluid-only simulations. In particular, to evaluate force and torque contributions from all intersecting lattice links, an intersection test must be performed between each link segment and the triangle mesh. Although these intersection tests can be accelerated using spatial data structures such as BVHs, they still require a large number of registers, increase instruction footprint, and induce severe warp divergence on GPUs. Threads near solid boundaries follow distinct execution paths involving geometric tests, boundary reconstruction, and additional memory accesses, reducing occupancy and parallel efficiency.

4.2 GPU-Friendly Computation Scheme

To alleviate the solid-coupling bottleneck, we propose a redesigned HOME-LBM computation pipeline that decouples fluid evolution and solid boundary handling into two kernels: a fluid update kernel and a solid boundary correction kernel. This separation makes the performance of the fluid update stage largely independent of solid geometry complexity. In addition, instead of the classical streaming \rightarrow collision ordering, we adopt a collision \rightarrow streaming scheme, which allows solid effects to be applied later as additive corrections in a separate kernel.

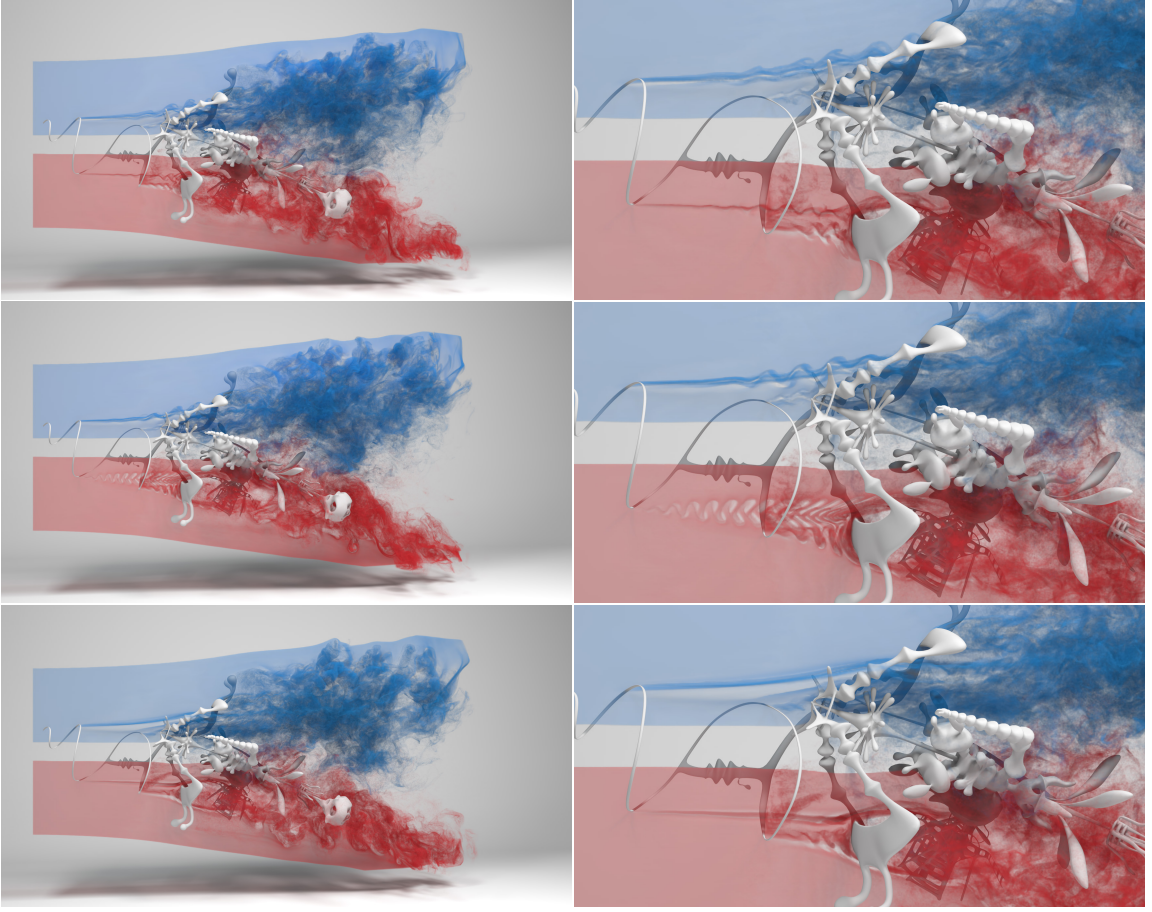


Fig. 6. 3D Yeahright. Comparison of flow simulations using different lattice velocity models and mesh resolutions, including D3Q27 with a low-resolution mesh, D3Q27 with a high-resolution mesh, and D3Q19 with a high-resolution mesh.

Fluid update kernel. In the first kernel, all lattice nodes are processed uniformly to advance the fluid dynamics, independent of the presence of solid boundaries. The kernel begins by fetching the moment variables ρ , $\rho\mathbf{u}$, and $\rho\mathbf{S}$, after which the moment-based collision operator is applied to obtain the post-collision moments ρ^+ , $(\rho\mathbf{u})^+$, and $(\rho\mathbf{S})^+$. These moments are then used to reconstruct the post-collision distribution functions f^+ , which are streamed to neighboring lattice nodes. Integrating the moment-based collision and distribution reconstruction into a single kernel function reduces register pressure on the GPU, thereby enhancing computational efficiency. The streamed distributions are used to reconstruct the updated moments, which are then written back to global memory. Because this kernel performs no solid-intersection tests or boundary handling, all threads within a warp follow identical execution paths and access memory in a regular lattice pattern, maximizing thread efficiency and overall GPU throughput.

Solid correction kernel. Since solid coupling is neglected in the fluid update kernel, a second kernel is launched to apply corrections induced by solid boundaries. Instead of launching over all lattice nodes, each triangle face of the solid geometry is assigned to one GPU thread, and only lattice nodes within the bounding box of each triangle are examined. Each lattice \mathbf{x} 's link is checked whether it intersects with the triangle T , and if so, the corresponding distributions are

Algorithm 1: Original HOME-LBM kernel

```

// Each GPU thread processes one lattice node  $x$ 
// Load moments and reconstruct distribution functions (Eq. 6)
1  $f^t \leftarrow \rho^t, \mathbf{u}^t, S^t$ 
2 for each lattice direction  $i$  do
3   | Intersection test between link  $l_i$  and obstacle
4   | if No intersection then
5   |   | // Streaming
6   |   |  $f_i^*(\mathbf{x}) \leftarrow f_i^t(\mathbf{x} - \mathbf{c}_i)$ 
7   | else
8   |   | // Coupling with solid
9   |   | Compute intersection point  $\mathbf{p}$ 
10  |   | Evaluate distribution function  $f^t(\mathbf{p})$  at intersection point  $\mathbf{p}$ 
11  |   |  $f_i^*(\mathbf{x}) \leftarrow f^t(\mathbf{p})$ 
10 end
11 // Reconstruct temporary moments (Eq. 5)
11  $\rho^*, \mathbf{u}^*, S^* \leftarrow f^*$ 
12 // Moment-based collision (Eq. 33) and write back
12  $\rho^{t+1}, \mathbf{u}^{t+1}, S^{t+1} \leftarrow \rho^*, \mathbf{u}^*, S^*$ 

```

Algorithm 2: Fluid update kernel

```

// Each GPU thread processes one lattice node  $x$ 
// Load moments and apply moment-based collision (Eq. 33)
1  $\rho^*, (\rho\mathbf{u})^*, (\rho S)^* \leftarrow \rho^t, (\rho\mathbf{u})^t, (\rho S)^t$ 
// Reconstruct distribution functions (Eq. 6)
2  $f^* \leftarrow \rho^*, (\rho\mathbf{u})^*, (\rho S)^*$ 
// Streaming
3 for each lattice direction  $i$  do
4   |  $f_i(\mathbf{x}) \leftarrow f_i^*(\mathbf{x} - \mathbf{c}_i)$ 
5 end
// Reconstruct temporary moments (Eq. 5) and write back
6  $\rho^{t+1}, (\rho\mathbf{u})^{t+1}, (\rho S)^{t+1} \leftarrow f$ 

```

reconstructed using the solid velocity and stress tensor. Then, we compute a distribution function correction term $\Delta f_i(\mathbf{x}) = f_i(\mathbf{p}) - f_i(\mathbf{x} - \mathbf{c}_i)$, where \mathbf{p} denotes the boundary intersection position. The corrections are then projected back into moment space to obtain incremental updates $\Delta\rho$, $\Delta(\rho\mathbf{u})$, and $\Delta(\rho S)$, which are added to the global memory of moments produced by the previous fluid update kernel. Since multiple faces may contribute to the same lattice node, these moment corrections are accumulated into the global moment fields using `AtomicAdd`. Such updates occur only near solid boundaries, so the number of atomic operations is small compared to the total number of lattice updates.

Accelerating solid intersection test. Because each GPU thread would otherwise iterate over all lattice nodes within a triangle's bounding box and perform link-triangle intersection tests, a naive implementation results in a large number of redundant intersection evaluations. To mitigate this overhead while keeping the number of kernel launches minimal, we introduce an additional preprocessing step that voxelizes the solid surface and marks lattice nodes containing surface triangles. During traversal of the bounding box, empty lattice nodes can be efficiently skipped, substantially reducing unnecessary intersection tests and improving overall performance.

Algorithm 3: Solid correction kernel

```

1 // Each GPU thread processes one triangle  $T$ 
2 for each triangle  $T$  do
3   for each lattice node  $\mathbf{x}$  within  $T$ 's bounding box do
4     for each lattice direction  $i$  do
5       Intersection test between link  $l_i$  and triangle  $T$ 
6       if No intersection then
7          $\Delta f_i(\mathbf{x}) \leftarrow 0$ 
8       else
9         // Load moments at  $\mathbf{x} - \mathbf{c}_i$  and recover
10        // distribution function (Eq. 6)
11         $f_i(\mathbf{x} - \mathbf{c}_i) \leftarrow \rho, \rho\mathbf{u}, \rho\mathbf{S}$ 
12        // Coupling with solid
13        Evaluate  $f(\mathbf{p})$  at intersection point  $\mathbf{p}$ 
14        // Compute distribution correction
15         $\Delta f_i(\mathbf{x}) \leftarrow f(\mathbf{p}) - f_i(\mathbf{x} - \mathbf{c}_i)$ 
16      end
17      // Reconstruct moments correction (Eq. 5)
18       $\Delta\rho, \Delta(\rho\mathbf{u}), \Delta(\rho\mathbf{S}) \leftarrow \Delta f$ 
19      // Update moments
20      AtomicAdd( $\rho^{t+1}, \Delta\rho$ )
21      AtomicAdd( $(\rho\mathbf{u})^{t+1}, \Delta(\rho\mathbf{u})$ )
22      AtomicAdd( $(\rho\mathbf{S})^{t+1}, \Delta(\rho\mathbf{S})$ )
23    end
24  end
25 end

```

Data layout. To further improve memory efficiency and access coherence, fluid nodes are stored in a structure-of-arrays (SoA) layout [Chen et al. 2022] and organized into fixed-size $8 \times 8 \times 8$ tiles. This layout scheme improves spatial locality when accessing boundary-adjacent fluid nodes and enables coalesced memory access during solid correction.

5 Stability-Guided Moment Quantization

To further reduce the runtime memory cost, we develop a stability-guided quantization strategy for HOME-LBM. Our key insight is that the allowable quantization error of each moment component is fundamentally constrained by the numerical stability of the underlying collision-streaming operator. We therefore perform the first von Neumann stability analysis of HOME-LBM to characterize the sensitivity of individual moments and derive principled stability bounds, which in turn guide bit allocation and quantization design.

5.1 Standard Stability Analysis of LBM

The standard von Neumann stability analysis for LBM [Sterling and Chen 1996] is a linear Fourier-mode analysis used to determine whether small perturbations in the distribution functions grow or decay under the discrete streaming–collision update. The method linearizes the dynamics around a uniform equilibrium state, assumes plane-wave perturbations, and yields an amplification matrix \mathbf{G} whose eigenvalues depend on the wave vector to explain LBM stability constraints. In our setting, we use the spectral radius and eigenvalue envelopes of \mathbf{G} to quantify the stability margins of individual moment components, which will later guide quantization design and bit allocation. A more detailed review of the classical VN formulation of LBM is provided in [Chávez-Modena et al. 2018]. Here, we only summarize the key elements required for extending the analysis to HOME-LBM.

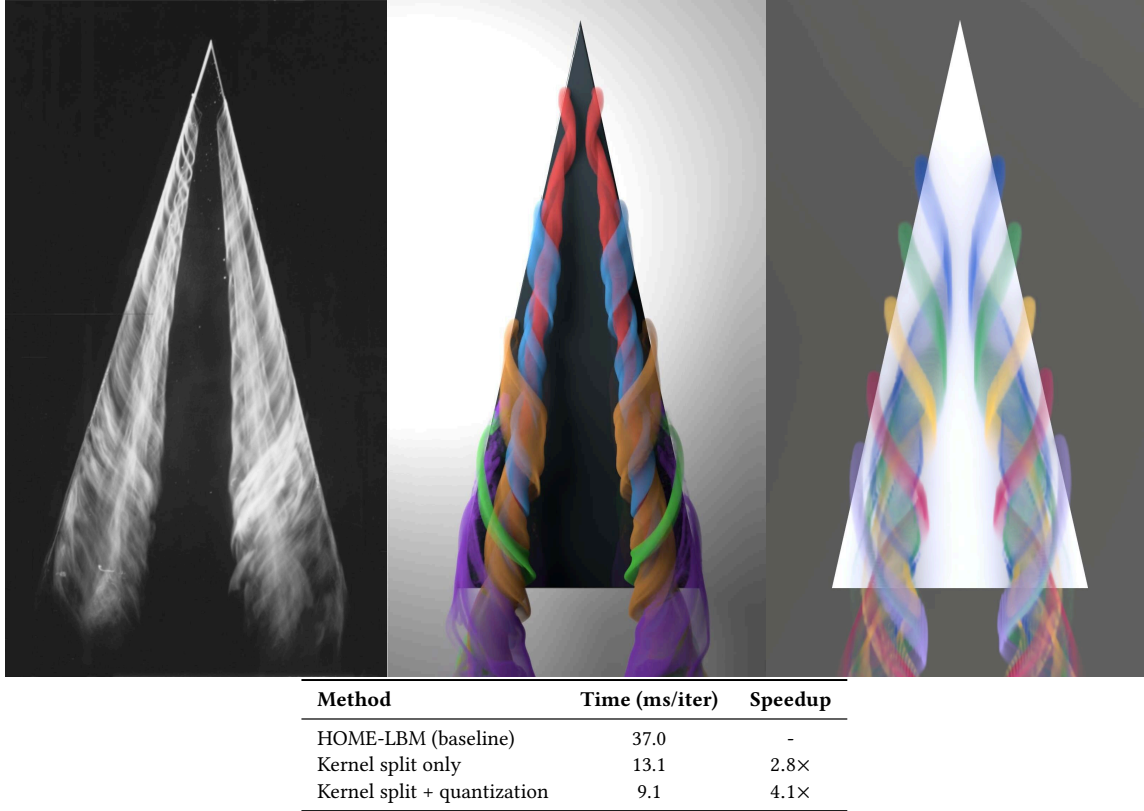


Fig. 7. 3D Delta Wing Comparison with Speedup Attribution. Airflow over a thin-shell delta wing simulated using our quantized kinetic solver (right) at a grid resolution of $660 \times 250 \times 330$, achieving $4.1\times$ speedup over HOME-LBM, with $2.8\times$ contributed by the split-kernel design and additional gains from 16-bit quantization. The simulation reproduces the characteristic spiral vortex structures forming near the leading edges of the wing. Results are shown in comparison with experimental flow visualization reported by [Délery 2001] (left) and HOME-LBM [Li et al. 2023] (middle).

5.1.1 General Collision–Streaming Update. Starting from the lattice Boltzmann equation (Eq. 2) and following Sterling and Chen [1996] to neglect the external force term for clarity, the discrete kinetic update can be written as:

$$f_i(\mathbf{x} + \mathbf{c}_i, t + 1) = f_i(\mathbf{x}, t) + \Omega_i(\mathbf{f}), \quad (9)$$

where Ω_i is the discrete collision term. We define the post-collision mapping

$$g_i(\mathbf{f}) = f_i + \Omega_i(\mathbf{f}), \quad (10)$$

so that the update becomes:

$$f_i(\mathbf{x} + \mathbf{c}_i, t + 1) = g_i(f(\mathbf{x}, t)). \quad (11)$$

5.1.2 Linearization via Perturbation and Jacobians. To analyze stability, we introduce a small perturbation around a spatially uniform equilibrium distribution:

$$f_i(\mathbf{x}, t) = \bar{f}_i + f'_i(\mathbf{x}, t), \quad \text{with} \quad |\bar{f}_i| \gg |f'_i|. \quad (12)$$

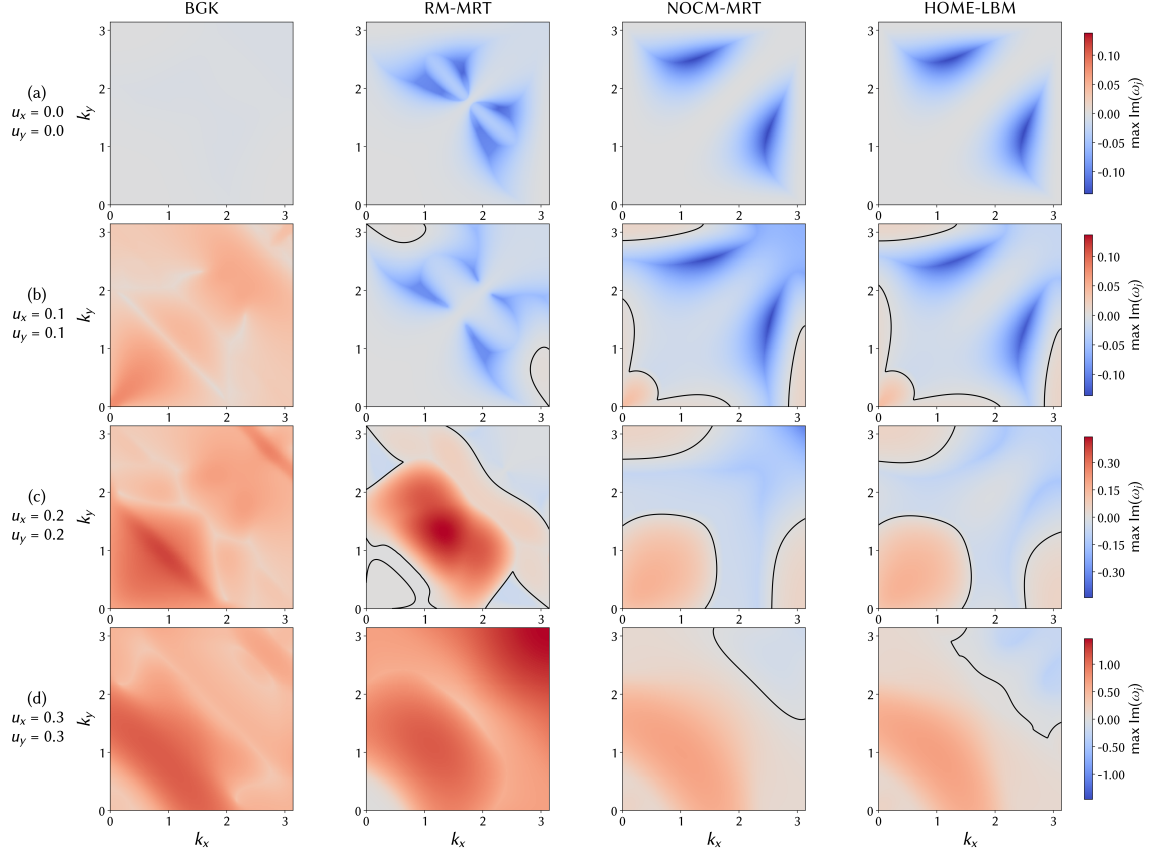


Fig. 8. Spectral Comparison of Maximal Dissipation across Collision Models. The maximal imaginary part of the eigenvalues, $\max \text{Im}(\omega_i)$, is visualized over the Fourier wavenumber space (k_x, k_y) for four collision models: BGK, RM-MRT, NOCM-MRT, and the HOME-LBM. (columns). Rows (a-d) correspond to increasing background velocities $(u_x, u_y) = (0, 0), (0.1, 0.1), (0.2, 0.2), (0.3, 0.3)$. Warmer colors indicate larger positive dissipation (unstable area), while cooler colors indicate negative or weakly dissipative modes (unconditionally stable area). Black contours denote the neutral stability boundary where $\max \text{Im}(\omega_i) = 0$.

where \bar{f}_i denotes the globally uniform equilibrium distribution that does not vary with time and space and $f'_i(\mathbf{x}, t)$ at node \mathbf{x} and time t accounts for a small perturbation from \bar{f}_i . Performing the first-order Taylor expansion of g_i around the equilibrium distribution \bar{f}_i with a small perturbation f'_i yields:

$$g_i(\bar{f} + f') \approx g_i(\bar{f}) + \sum_j \frac{\partial g_i}{\partial f_j} \bigg|_{\bar{f}} f'_j. \quad (13)$$

To proceed, we note that most practical LBM collision models can be interpreted as linear relaxation of moments toward their equilibrium values [Higuera and Jiménez 1989]. When expressed in distribution-function space, this relaxation admits the unified matrix representation:

$$\Omega(\mathbf{f}) = \mathbf{K}(\mathbf{f}^{eq} - \mathbf{f}), \quad (14)$$

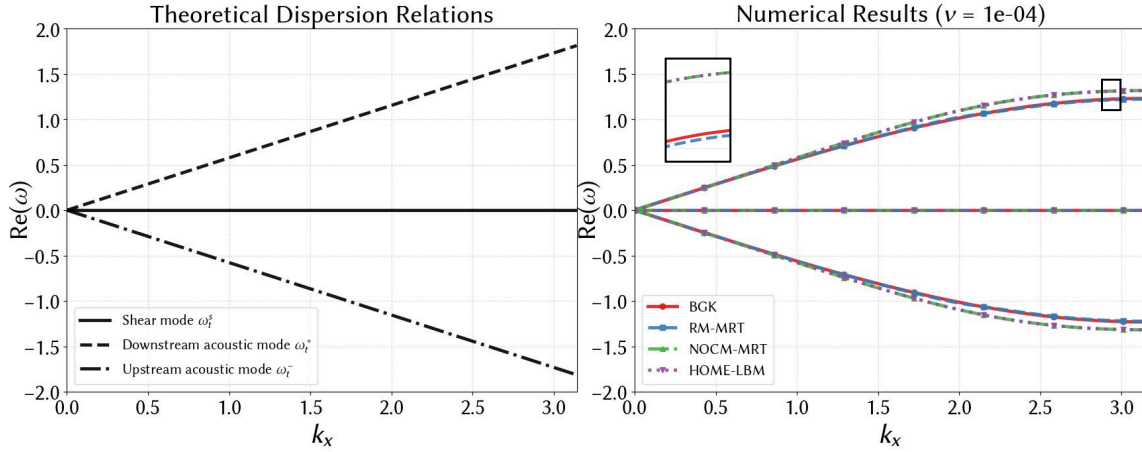


Fig. 9. Comparison of Dispersion across Different Collision Models. Left: theoretical dispersion relations of the shear mode and the upstream and downstream acoustic modes. Right: numerical dispersion curves at $v = 10^{-4}$ for BGK [Chen and Doolen 1998], RM-MRT [d'Humieres 1992], NOCM-MRT [De Rosis 2017], and the HOME-LBM [Li et al. 2023], obtained from eigenvalue analysis.

where the collision matrix \mathbf{K} characterizes how the distribution function relaxes toward its equilibrium state. Therefore, the linearized evolution becomes:

$$g_i(\bar{f} + f') = \bar{f}_i + f'_i(\mathbf{x}, t) + \mathbf{K}_{ij} \left(\Lambda_{ij} f'_j(\mathbf{x}, t) - f'_i(\mathbf{x}, t) \right) \quad (15)$$

where Λ is the Jacobian of the equilibrium distribution with elements

$$\Lambda_{ij} = \frac{\partial f_i^{eq}}{\partial \rho} \frac{\partial \rho}{\partial f_j} + \sum_{\alpha} \frac{\partial f_i^{eq}}{\partial u_{\alpha}} \frac{\partial u_{\alpha}}{\partial f_j}. \quad (16)$$

We provide detailed derivations and explicit expressions of the Jacobian matrices in [Appendix E](#). Combining [Eq. 12](#) and [Eq. 13](#), the evolution of the perturbation is given by:

$$f'_i(\mathbf{x} + \mathbf{c}_i, t + 1) = \left[\mathbf{I} + \mathbf{K}(\Lambda - \mathbf{I}) \right]_{ij} f'_j(\mathbf{x}, t). \quad (17)$$

This equation defines a linear dynamical system and serves as the starting point for the subsequent Fourier (von Neumann) stability analysis.

5.1.3 Plane-Wave Substitution and Amplification Matrix. Following standard VN analysis [Eq. 17](#), we assume a plane-wave solution of the form [Wissocq et al. 2020]:

$$f'_i(\mathbf{x}, t) = \hat{f}_i e^{i(\mathbf{k} \cdot \mathbf{x} - \omega t)}, \quad (18)$$

where \hat{f}_i denotes the complex amplitude, and the exponential term represents a monochromatic plane wave with wave vector \mathbf{k} and angular frequency ω . The imaginary unit satisfies $i^2 = -1$. Combining the streaming phase factor with the Jacobian operator yields the amplification matrix $\mathbf{G}(\mathbf{k})$:

$$\mathbf{G}(\mathbf{k}) = \mathbf{D}(\mathbf{k}) [\mathbf{I} + \mathbf{K}(\Lambda - \mathbf{I})], \quad (19)$$

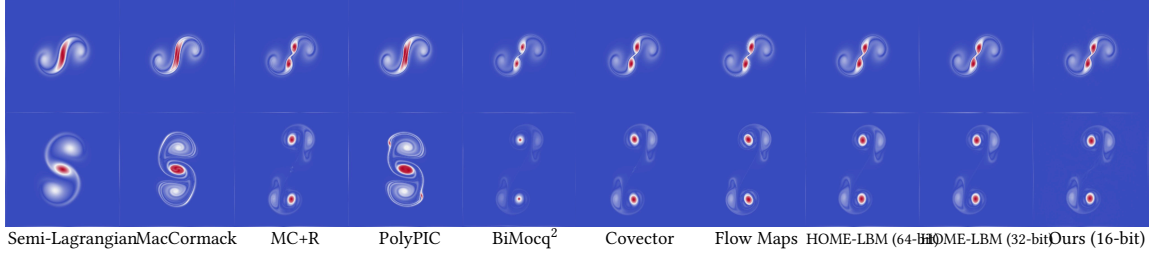


Fig. 10. 2D Taylor Vortex Comparison. Comparison of vorticity advection results using Semi-Lagrangian [Stam 1999], MacCormack [Selle et al. 2008], MC+R [Zehnder et al. 2018], PolyPIC [Fu et al. 2017], BiMocq² [Qu et al. 2019], Covector [Nabizadeh et al. 2022], and flow maps [Wang et al. 2024]. We additionally include HOME-LBM [Li et al. 2023] baselines using full-precision double (64-bit) and single-precision float (32-bit) variants, as well as our 16-bit quantized solver. All methods use the same grid resolution of 256×256 .

where $\mathbf{D}(\mathbf{k}) = \text{diag}(e^{-i\mathbf{k} \cdot \mathbf{c}_0}, \dots, e^{-i\mathbf{k} \cdot \mathbf{c}_{q-1}})$ represents the advection operator in Fourier space. \mathbf{K} and Λ correspond to the collision and jacobian matrices, respectively. This matrix $\mathbf{G}(\mathbf{k})$ compactly encodes the linearized evolution of Fourier modes and provides a convenient basis for analyzing the stability, dispersion, and numerical properties of the scheme.

5.2 Stability Analysis of HOME-LBM

5.2.1 HOME-LBM Reconstruction Mapping. In HOME-LBM, the post-collision distribution is not stored explicitly. Instead, the final distribution is reconstructed from a reduced set of velocity moments using a third-order Hermite expansion. As a result, the effective update mapping differs from standard distribution-based LBM. Specifically, we express the HOME-LBM update as a composition of moment extraction, collision, and distribution function reconstruction, which can be written as :

$$g^{\text{HOME}}(\mathbf{f}) = \mathbf{h}(\mathbf{m}(\mathbf{f}^+)), \quad (20)$$

where $\mathbf{h}()$ performs Hermite reconstruction of the distribution, $\mathbf{m}(\mathbf{f}) \doteq (\rho, \mathbf{u}, \mathbf{S})$ represents the moment reconstruction in Eq. 5 and intermediate post-collision \mathbf{f}^+ is obtained by applying the underlying NOCM-MRT collision step to \mathbf{f} :

$$\mathbf{f}^+ = \mathbf{f} + \Omega^{\text{NOCM-MRT}}(\mathbf{f}) = \mathbf{f} - \mathbf{M}^{-1} \mathbf{R} \mathbf{M} (\mathbf{f} - \mathbf{f}^{\text{eq}}), \quad (21)$$

where \mathbf{M} is the moment projection matrix in NOCM-MRT collision model, and \mathbf{R} is a diagonal matrix of relaxation rates $\{r_i\}_{i=1 \dots q}$ [Li et al. 2020]. This ‘‘moment representation + reconstruction’’ procedure first converts the post-collision distribution into a set of moments, and then reconstructs the distribution by projecting it onto a truncated third-order Hermite subspace. While this reconstruction is algebraically equivalent for macroscopic dynamics, it alters the effective linearized update operator and consequently impacts numerical stability and error amplification.

5.2.2 Linearization of the Composite Mapping. Following the standard perturbation and linearization procedure introduced in Sec. 5.1, we linearize the composite mapping g^{HOME} around a uniform equilibrium and analyze its Jacobian with respect to the distribution function. Since g^{HOME} is a composition of moment extraction, collision, and reconstruction operators, its Jacobian follows directly from the chain rule.

To obtain a closed-form expression of the Jacobian, we exploit the Hermite-based decomposition of the distribution function under the Chapman–Enskog expansion assumption [Malaspina 2015] and express it as the sum of equilibrium

and non-equilibrium components:

$$f = f^{\text{eq}} + f^{\text{neq}}. \quad (22)$$

. Following prior analysis [Malaspinas 2015], the zeroth- and first-order non-equilibrium Hermite coefficients vanish, i.e., $\mathbf{a}^{[0],\text{neq}} = 0$ and $\mathbf{a}^{[1],\text{neq}} = 0$ and the non-equilibrium distribution can be expressed using second- and third-order Hermite components:

$$f^{\text{neq}} = \mathbf{A}_2 \mathbf{a}^{[2],\text{neq}} + \mathbf{A}_3 \mathbf{a}^{[3],\text{neq}}, \quad (23)$$

where $\mathbf{A}_2 \in \mathbb{R}^{9 \times 3}$ and $\mathbf{A}_3 \in \mathbb{R}^{9 \times 4}$ collect the discrete Hermite basis contributions. Exploiting the recursive structure in [Malaspinas 2015], the third-order non-equilibrium coefficient can be expressed as: $\mathbf{a}^{[3],\text{neq}} = \mathbf{R}_u \mathbf{a}^{[2],\text{neq}}$, which allows Eq. 23 to be rewritten in the compact form:

$$f^{\text{neq}} = \mathbf{Q}_u \mathbf{a}^{[2],\text{neq}}, \quad (24)$$

where $\mathbf{Q}_u = \mathbf{A}_2 + \mathbf{A}_3 \mathbf{R}_u$ and recursive matrix $\mathbf{R}_u \in \mathbb{R}^{4 \times 3}$ in 2D and $\mathbb{R}^{10 \times 6}$ in 3D.

As noted by Li et al. [2023], the second-order Hermite coefficient satisfies $\mathbf{a}^{[2]} = \rho \mathbf{S} = \mathbf{B} \mathbf{f}$ and $\mathbf{a}^{[2],\text{eq}} = \rho \mathbf{S}^{\text{eq}} = \mathbf{B} \mathbf{f}^{\text{eq}}$, which yields:

$$\mathbf{a}^{[2],\text{neq}} = \rho(\mathbf{S} - \mathbf{S}^{\text{eq}}) = \mathbf{B}(\mathbf{f}^+ - \mathbf{f}^{\text{eq}}), \quad (25)$$

where the matrix $\mathbf{B} \in \mathbb{R}^{3 \times 9}$ in 2D and $\mathbb{R}^{6 \times 27}$ in 3D is a constant projection matrix mapping distribution functions to second-order moment components; its entries are defined symbolically in terms of the lattice velocities \mathbf{c} and the lattice sound speed c_s .

Substituting the above relation (Eq. 25) into the compact expression of f^{neq} (Eq. 24) and replacing the non-equilibrium component in the decomposition of f (Eq. 22) yields the first-order variation of the reconstructed distribution:

$$g_i = \bar{f}_i + [\mathbf{Q}_u \mathbf{B}(\mathbf{f}^+ - \mathbf{f}^{\text{eq}})]_i, \quad (26)$$

Finally, substituting \mathbf{f}^+ given in Eq. 21 into the above expression Eq. 26 gives:

$$g_i = \bar{f}_i + \left[\mathbf{Q}_u \mathbf{B} \left(\mathbf{f} - \mathbf{M}^{-1} \mathbf{R} \mathbf{M}(\mathbf{f} - \mathbf{f}^{\text{eq}}) - \mathbf{f}^{\text{eq}} \right) \right]_i. \quad (27)$$

This expression explicitly defines the Jacobian operator of the HOME-LBM composite mapping evaluated at equilibrium.

The amplification matrix \mathbf{G} of the HOME-LBM can be accordingly written as:

$$\mathbf{G}_{ij} = e^{-i\mathbf{k} \cdot \mathbf{c}_i} [\mathbf{A} + \mathbf{Q}_u \mathbf{B} (\mathbf{I} - \mathbf{M}^{-1} \mathbf{R} \mathbf{M}(\mathbf{I} - \mathbf{A}) - \mathbf{A})]_{ij}. \quad (28)$$

The explicit forms of the matrices \mathbf{A}_2 , \mathbf{A}_3 , \mathbf{R}_u , \mathbf{B} , as well as their dimensions, are provided in Appendix D.

5.3 Numerical Spectral Analysis

To validate our theoretical stability analysis and compare the spectral behavior of different collision models, we conduct three sets of numerical experiments involving four schemes: BGK [Chen and Doolen 1998], RM-MRT [d'Humieres 1992], NOCM-MRT [De Rosis 2017], and HOME-LBM [Li et al. 2023].

Stability margin. As shown in Fig. 8, we evaluate the maximum modulus of eigenvalues, $\max |\lambda(\mathbf{k})|$, of the amplification matrix \mathbf{G} as a function of the wave number k_x , under three different kinematic viscosities: $\nu = 10^{-3}$, 10^{-4} , and 10^{-5} . According to the von Neumann criterion, stability requires $|\lambda(\mathbf{k})| \leq 1$ for all wave vectors. BGK exhibits noticeably stronger damping at intermediate wave numbers, reflected by significantly smaller values of $\max |\lambda|$. This indicates

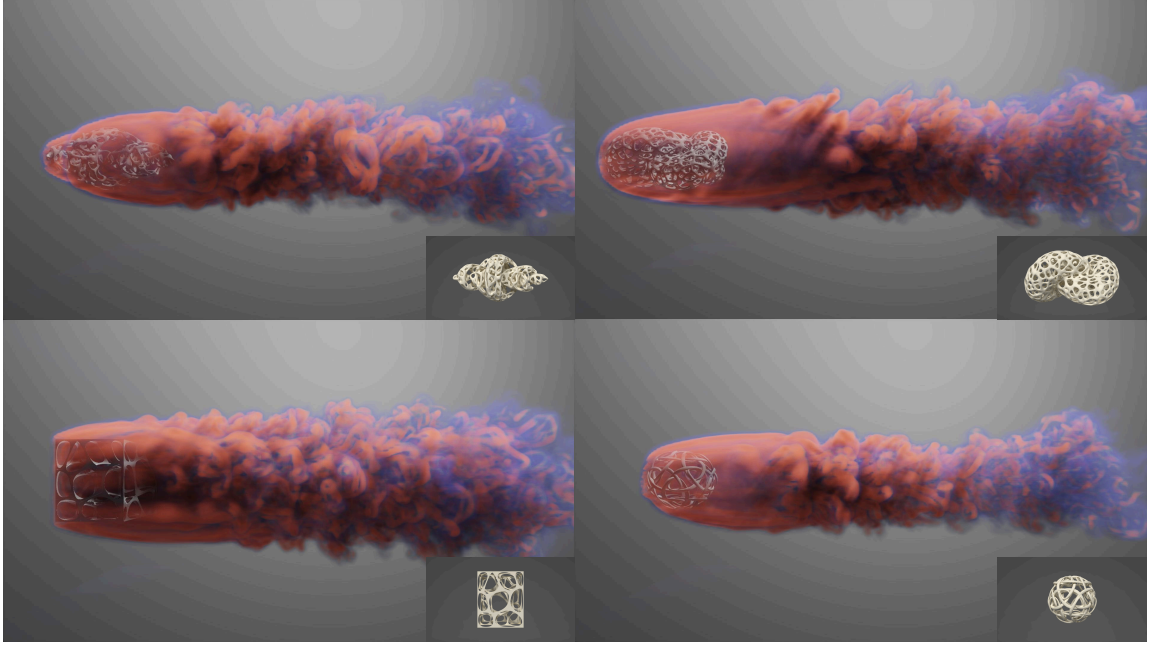


Fig. 11. Real-Time Flow Through Complex Porous Structures. Real-time 3D smoke simulations interacting with a set of porous solids exhibiting diverse micro-geometry.

excessive numerical dissipation, which is known to suppress vortical structures and fine-scale details. RM-MRT improves stability over BGK in certain wave-number ranges but exhibits irregular spectral behavior near high-frequency modes, suggesting reduced robustness under low-viscosity conditions. In contrast, both NOCM-MRT and HOME-LBM maintain eigenvalues much closer to the unit circle across the entire spectrum. Importantly, HOME-LBM almost perfectly overlaps with the full NOCM-MRT model, indicating that the reconstruction error of third-order Hermite-based distribution construction exerts a negligible impact on stability. This confirms that the distribution reconstruction in HOME-LBM maintains robust numerical performance without introducing additional instabilities.

Dissipation distribution in wave-number space. We visualize the two-dimensional maximal dissipation rate $\text{Im}(\omega)$ over the full wave-number domain $\mathbf{k} = (k_x, k_y) \in [0, \pi]^2$ in Fig. 8. For each wave vector, we evaluate the maximal imaginary part of the eigenvalues, $\max \text{Im}(\omega)$, which quantifies the strongest dissipation or growth rate among all modes. Regions that $\max \text{Im}(\omega) > 0$ correspond to linearly unstable modes (outlined by solid contours). We compare over four velocities: $\mathbf{u} = (0, 0), (0.1, 0.1), (0.2, 0.2)$, and $(0.3, 0.3)$, in order to assess the effect of increasing advection on numerical dissipation and stability.

NOCM-MRT remains stable over most of the wave-number domain, with dissipation primarily concentrated near compressible modes. HOME-LBM exhibits nearly identical dissipation and stability maps, with only minor deviations near extreme wave numbers. This demonstrates that moment encoding and third-order Hermite-based reconstruction do not introduce additional unstable modes and faithfully preserve the dissipation characteristics of the underlying NOCM-MRT formulation.

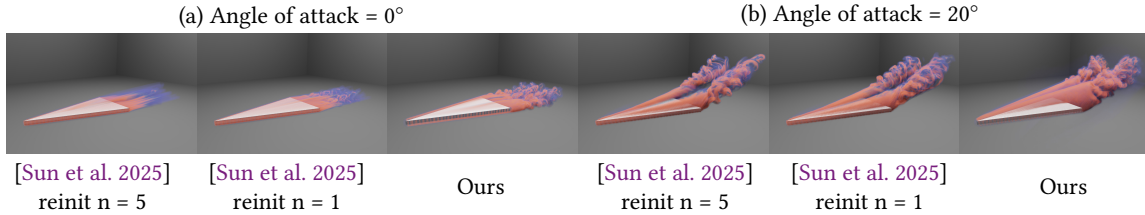


Fig. 12. Comparison of Flow over a Delta Wing at Different Angles of Attack. Qualitative comparison between our real-time 3D simulation and the Leapfrog FlowMap method by Sun et al. [2025] at a grid resolution of $256 \times 128 \times 128$. Two angles of attack are shown: (a) 0° and (b) 20° . For each angle, results from Sun et al. are shown with different reinitialization frequencies ($n = 5$ and $n = 1$), followed by our method. All simulations are rendered using the same visualization settings.

Dispersion Relations of Hydrodynamic Modes. The theoretical hydrodynamic modes are obtained by linearizing the Navier–Stokes equations around a uniform background flow [Jovanovic and Bamieh 2001]. The resulting eigenmodes consist of one shear mode ω_t^s and two acoustic modes ω_t^\pm , whose analytical expressions are given by:

$$\omega_t^s = |\mathbf{k}| |\mathbf{u}| \cos \phi - i |\mathbf{k}|^2 v, \quad (29)$$

$$\omega_t^\pm = |\mathbf{k}| (|\mathbf{u}| \cos \phi \pm c_s) - i |\mathbf{k}|^2 \left(\frac{D-1}{D} v + \frac{\mu_v}{2} \right), \quad (30)$$

where \mathbf{k} denotes the wave vector, ϕ is the angle between the perturbation direction and the background velocity \mathbf{u} , c_s is the sound speed, v is the kinematic viscosity, μ_v is the bulk viscosity, and D is the spatial dimension.

As shown in (Fig. 9), we compare numerical dispersion relations obtained from the amplification matrix with the theoretical predictions given by Eq. 29 and Eq. 30. We focus on the real part of ω and plot $\text{Re}(\omega)$ as a function of the wave number k_x for $v = 10^{-4}$.

The theoretical reference consists of a zero-frequency shear branch and two acoustic branches with slopes $\pm c_s$ in the long-wavelength limit. Consistent with this prediction, all schemes agree closely at low wave numbers, indicating negligible dispersion error in the hydrodynamic regime. As k_x increases, the acoustic branches exhibit increasing deviation from the linear theory, reflecting the expected numerical dispersion at under-resolved (high-frequency) scales.

Across the entire spectrum, the proposed HOME-LBM closely matches the full NOCM-MRT baseline, with nearly indistinguishable curves, confirming that third-order Hermite-based moment reconstruction does not introduce additional dispersion beyond that of the underlying collision model.

5.4 Stability-Guided Quantization Scheme

Moment range analysis. To enable fixed-point quantization, we determine conservative numerical ranges for each moment variable based on physical constraints and stability considerations of the underlying LBM scheme. In weakly compressible LBM, density fluctuations are expected to remain small around the reference value $\rho = 1$. As LBM is weakly compressible, we explicitly account for density variations. From an extreme-turbulence 3D flow-over-a-sphere experiment (Fig. 13) with setting (inlet velocity 0.256 and $v = 0$ and $512 \times 256 \times 256$ grid resolution), we find that the density varies within $\rho \in [0.8, 1.5]$, even in highly vortical regions. To avoid compressibility artifacts and numerical instability according to Fig. 8, we adopt a conservative velocity bound $u \in [-0.4, 0.4]$, chosen as the smallest interval that still contains the maximum speeds observed across all benchmarks and lies safely within the stability region predicted by the von Neumann analysis, thereby improving following quantization precision.

Range reduction of ρS . For second-order moments ρS , we further reduce the dynamic range by exploiting the decomposition of the stress tensor into equilibrium and non-equilibrium components. Specifically, the second-order moment tensor can be written as:

$$\rho S_{\alpha\alpha} = \rho S_{\alpha\alpha}^{neq} + \rho u_\alpha^2 + \rho c_s^2, \quad \rho S_{\alpha\beta} = \rho S_{\alpha\beta}^{neq} + \rho u_\alpha u_\beta \quad (\alpha \neq \beta). \quad (31)$$

We only store high-frequency non-equilibrium components that exhibit a progressively smaller amplitude in multiscale perturbation analysis [Harris 2004] and are particularly amenable to quantization:

$$\rho S_{\alpha\alpha}^{neq} = \rho S_{\alpha\alpha} - \rho u_\alpha^2 - \frac{1}{3}, \quad \rho S_{\alpha\beta}^{neq} = \rho S_{\alpha\beta} - \rho u_\alpha u_\beta \quad (\alpha \neq \beta). \quad (32)$$

This exhibits reduced dynamic ranges from $[-0.1, 0.6]$ to $[-0.1, 0.1]$ and effectively increases the quantization resolution of second-order moments by more than a factor of three at the same bit width. This design is also consistent with the stability analysis, which indicates that dissipation and stability properties are primarily governed by second-order non-equilibrium moments, while equilibrium components contribute mainly to macroscopic transport and can be reconstructed analytically without loss of stability.

Normalization and fixed-point quantization. Each moment component m is normalized to a unit interval using: $m' = \frac{m - m_{\min}}{m_{\max} - m_{\min}}$, where m_{\min} and m_{\max} denote the predefined bounds derived from the range analysis in the previous paragraph. This normalization maps all stored moments to the range $[0, 1]$. After normalization, each moment component is quantized into a b -bit unsigned integer using uniform quantization: $q(m) = \lfloor m' (2^b - 1) + \frac{1}{2} \rfloor$, with dequantization performed by the inverse mapping $\hat{m} = m_{\min} + q(m) \left(\frac{m_{\max} - m_{\min}}{2^b - 1} \right)$, which approximates the original value m up to quantization error. In our implementation, most moment components are stored using 16-bit fixed-point integers ($b = 16$), allowing two moments to be packed into a single 32-bit word. Consequently, the moment buffer requires five uint32 values per lattice node instead of ten float32 values, reducing both memory footprint and global memory write bandwidth by approximately 50%.

Dithering. To reduce potential bias introduced by deterministic rounding, we apply spatial dithering during quantization. Specifically, a small zero-mean noise uniformly distributed in $[-\frac{1}{2}, \frac{1}{2}]$ of one quantization unit [Liu et al. 2022b] is added to the normalized value prior to rounding. This converts deterministic rounding error into zero-mean stochastic noise, thereby preventing systematic bias accumulation over long time integration.

Atomic accumulation with mixed precision. When solid coupling is present, multiple triangle faces may contribute moment corrections to the same lattice node, which requires atomic accumulation of moment updates in the solid correction kernel. Performing atomic operations directly on quantized fixed-point values would introduce order-dependent rounding errors and may lead to noticeable bias accumulation over long simulations. To mitigate this issue, we adopt a mixed-precision strategy. Specifically, we maintain two moment buffers: a full-precision moment buffer storing post-streaming moments using 32-bit floating-point values, and a quantized moment buffer storing post-collision moments in fixed-point format. The solid correction kernel accumulates moment corrections using atomicAdd on the full-precision buffer, ensuring numerically stable and order-independent accumulation. After all solid corrections are applied, the corrected moments are re-quantized and written back to the compact fixed-point buffer for the next fluid update step. Since only the post-collision moment buffer is quantized, the overall memory reduction is approximately 25% compared to the full-precision implementation, which we find to be a favorable trade-off between accuracy and bandwidth savings in solid-coupled simulations.

6 Results

6.1 Implementation Details

Most experiments are conducted on a workstation equipped with an AMD Ryzen Threadripper 3970X 32-core processor and a single GPU with 16,384 cores and 24 GB of memory. Large-scale fluid-only simulations (Fig. 3) are executed on a single GPU with 6,912 cores and 80 GB memory. All algorithms are implemented in CUDA and compiled on both Windows and Ubuntu 22.04.

We summarize per-scene statistics in Table 1, which include only simulation unless otherwise specified. When solids are present, we additionally report mesh complexity and relevant computation costs. Unless stated otherwise, all per-iteration timings are reported in milliseconds, measured using GPU profiling tool after a short warm-up phase to exclude initialization overhead. Total execution time is reported in seconds. For real-time visualization, we employ the Vulkan-based ray-marching volume renderer from [Sun et al. 2025], enabling direct rendering from GPU simulation buffers. For high-quality offline rendering, particle data are exported, converted to volumetric representations using openVDB library [Museth et al. 2025], and rendered in Cinema 4D using Redshift [Maxon 2026].

6.2 Moment Quantization

We evaluate the impact of fixed-point quantization on memory footprint and numerical accuracy.

6.2.1 2D Taylor Vortex. We evaluate long-term vortex evolution using the 2D Taylor vortex benchmark, following the setup in prior work [Nabizadeh et al. 2022; Qu et al. 2019]. We compare against representative grid-based and particle-based fluid solvers, including Semi-Lagrangian [Stam 1999], MacCormack [Selle et al. 2008], MC+R [Zehnder et al. 2018], PolyPIC [Fu et al. 2017], BiMocq² [Qu et al. 2019], Covector [Nabizadeh et al. 2022], and flow maps [Wang et al. 2024], as well as HOME-LBM [Li et al. 2023] baselines using double precision (64-bit) and single precision (32-bit). All methods use identical grid resolution 256×256 . As shown in Fig. 10, classical semi-Lagrangian schemes exhibit progressive vortex-core diffusion, while particle-based methods preserve sharper structures with increased high-frequency artifacts. In contrast, HOME-LBM preserves coherent vortex structures with limited diffusion. Our 16-bit quantized solver remains visually consistent with the 64-bit and 32-bit HOME-LBM baselines and closely matches the results produced by other high-quality advection methods, indicating that the proposed moment-space quantization preserves visual fidelity and numerical behavior while reducing memory cost by 50%.

6.2.2 2D Double-Layer Vortex. Guided by the stability analysis in Sec. 5, we adopt an adaptive bit-allocation strategy to balance quantization error across moment components. Since density and velocity exhibit similar normalized ranges and directly affect macroscopic transport, we assign the same bit-width to ρ and $\rho\mathbf{u}$. In contrast, after range reduction, the non-equilibrium stress moments $\rho\mathbf{S}^{\text{neq}}$ exhibit significantly smaller dynamic ranges and can therefore be represented with fewer bits. We denote a configuration as $b_{\rho\mathbf{u}}/b_{\mathbf{S}}$, where $b_{\rho\mathbf{u}}$ and $b_{\mathbf{S}}$ are the bit-widths for density–velocity and stress moments, respectively. For example, the 16/15 configuration stores ρ and $\rho\mathbf{u}$ using 16 bits and stores $\rho\mathbf{S}^{\text{neq}}$ using 15 bits. As shown in Fig. 14, this balanced allocation yields a smooth accuracy–memory trade-off. Reducing stress precision to 14–15 bits introduces only minor error increases, whereas a more aggressive reduction leads to rapid degradation in both numerical accuracy and visual quality.

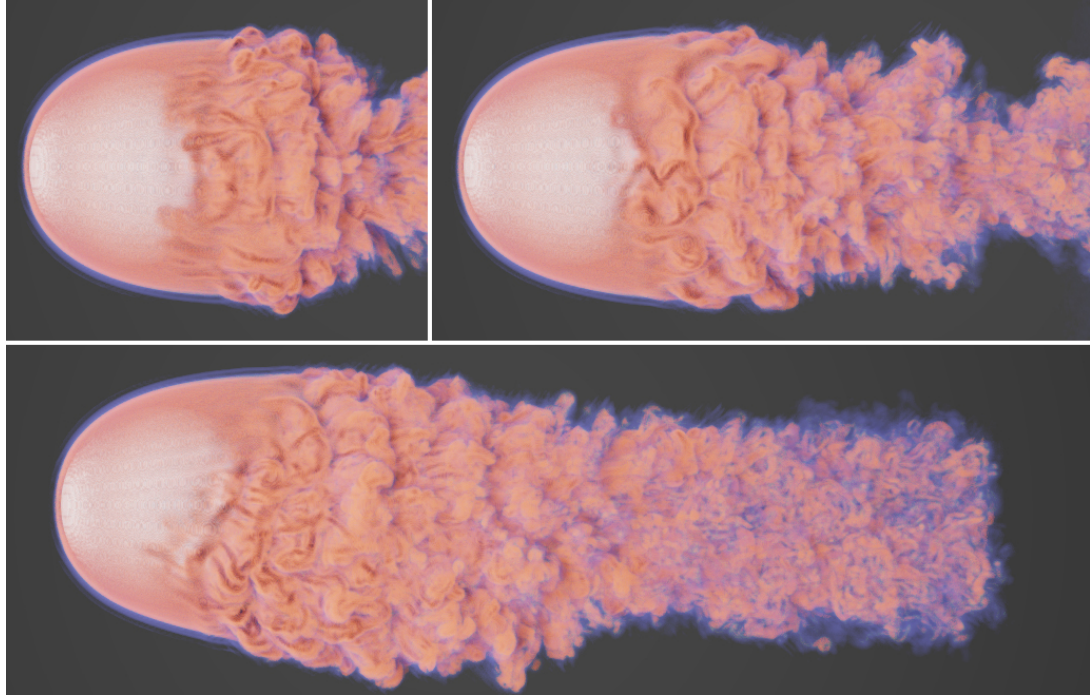


Fig. 13. Turbulent 3D flow over a sphere As LBM is weakly compressible, we explicitly account for density variations. This experiment ($v = 0$) provides the maximal range observed in fluid density for quantization.

6.3 Effect of GPU-Oriented optimizations

6.3.1 End-to-End performance comparison with HOME-LBM. We compare the end-to-end simulation performance of our GPU-oriented HOME-LBM implementation with the original single-kernel HOME-LBM algorithm [Li et al. 2023]. Both implementations use identical collision models, boundary conditions, and time step sizes. In terms of memory footprint, the proposed solver reduces storage by approximately 50% in fluid-only simulations and 25% in fluid–solid coupling scenarios. From a computational perspective, the fluid update stage benefits from reduced memory access and improved memory locality, while the solid correction stage avoids warp divergence and limits execution to boundary-intersecting cells, significantly reducing unnecessary thread activity. As shown in Fig. 7, our method achieves 4.1× speedup in scenes with complex solid boundaries with similar spiral vortex forming near the edges of the wing.

6.3.2 Impact of Solid Complexity. To evaluate how performance scales with geometric complexity, we vary the number of triangle faces while keeping the fluid resolution fixed.

Yeahright. Fig. 6 shows a coupled fluid–solid simulation in which smoke flows through a humanoid skeleton under different lattice configurations and mesh resolutions. The three rows correspond to D3Q27 with a low-resolution mesh (top), D3Q27 with a high-resolution mesh (middle), and D3Q19 with a high-resolution mesh (bottom). The overall flow structure remains visually consistent across configurations; however, noticeable differences emerge primarily near fine geometric features, such as the slender rod elements of the skeleton. In these regions, higher mesh resolution with D3Q27 lattice structure produces more detailed and coherent vortical structures, whereas coarser discretizations tend to smooth or attenuate small-scale vorticity. From a performance perspective, increasing mesh complexity introduces

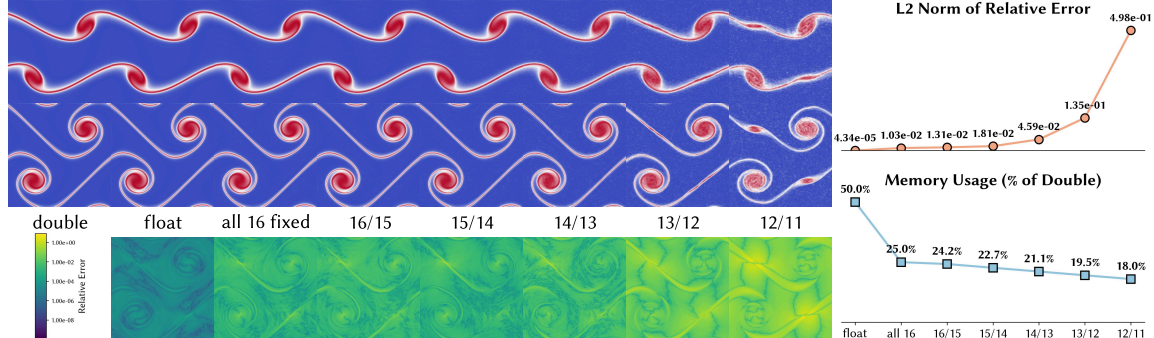


Fig. 14. 2D Double-Layer Vortex under Different Quantization Configurations. Top Left: vorticity snapshots for the 64-bit double-precision reference, 32-bit float, uniform fixed 16-bit quantization, and adaptive bit-allocation configurations $b_{pu}/b_S \in \{16/15, 15/14, 14/13, 13/12, 12/11\}$. Bottom Left: spatial distribution of the pointwise relative error with respect to the double-precision reference. Right: quantitative comparison of the accuracy-memory trade-off, measured by the ℓ_2 norm of the relative error and the memory usage normalized by the double-precision baseline.

substantial overhead in the original HOME-LBM due to the escalating costs of BVH intersection queries. In contrast, our decoupled two-pass formulation confines boundary processing to a sparse solid-correction stage, resulting in much slower growth in total runtime as the triangle count increases. This allows the solver to scale more robustly with geometric complexity while maintaining high throughput.

Hilbert Space-Filling Curve (SFC). To evaluate the robustness of our solver under highly intricate boundaries, we simulate flow past obstacles generated by 3D Hilbert curves with increasing iteration levels, as shown in Fig. 4. As the curve density increases, the resulting geometric complexity creates increasingly tortuous flow paths and higher hydraulic resistance. Our solver captures the resulting multi-scale vortical structures and turbulent cascades while maintaining favorable runtime scaling. We further observe a clear morphological change in the downstream wake: at higher curve densities, the wake exhibits an inward contraction driven by the increased pressure gradient induced by the densely packed obstacles, as illustrated in Fig. 4(d).

6.3.3 Performance Comparison with SOTA. We compare our method with the SOTA real-time fluid–solid coupling approach [Sun et al. 2025] using the 3D delta wing benchmark under two angles of attack, 0° and 20° , as shown in Fig. 12. All simulations are performed at a grid resolution of $256 \times 128 \times 128$ with identical boundary conditions, inflow settings, and visualization parameters. For each angle of attack, results from [Sun et al. 2025] are shown using two reinitialization frequencies, $n = 5$ and $n = 1$, followed by our method. The reinitialization frequency controls how often the velocity field is reset to suppress accumulated numerical errors in the Leapfrog Flow Map pipeline. Across both angles, all methods produce an attached flow regime with a mild wake structure near the trailing edge. As the reinitialization frequency decreases, the Leapfrog results exhibit progressively richer small-scale flow details, becoming visually closer to the structures produced by our solver. However, lower reinitialization frequencies also incur increased computational cost in the Leapfrog pipeline due to more frequent advection and correction steps. In contrast, our method consistently achieves comparable fine-scale detail while maintaining a $5.2\times$ speedup over the Leapfrog implementation at the same resolution and visualization settings.

6.4 Large-Scale Simulations

Fluid-only simulation. To demonstrate the scalability and fidelity of our solver at extreme resolutions, we simulate two cases of obliquely impacting jets on a 1024^3 grid at different Reynolds numbers, as shown in Fig. 3. At lower Reynolds numbers, the flow exhibits stable, coherent vortex structures, while at higher Reynolds numbers, the solver resolves fine-scale turbulent filaments and intermittent eddies across a wide range of spatial scales. Our quantized formulation reduces the memory footprint by 50% compared to full-precision baselines, enabling large-scale simulations that would otherwise exceed GPU memory capacity. This demonstrates that our framework can efficiently support high-resolution fluid simulations while preserving rich small-scale flow details.

Fluid–solid coupling simulation. We further demonstrate large-scale fluid–solid interaction using turbulent smoke simulations around a Ducati motorcycle and a Ferrari F1 racing car at a grid resolution of $1000 \times 400 \times 400$, as shown in Fig. 1 and Fig. 2. The simulations use 16-bit quantization and incorporate highly detailed solid geometry with intricate boundary features. Despite the large problem size and geometric complexity, the solver develops complex shear layers and coherent vortex structures while maintaining stable temporal evolution and consistent visual quality over long sequences, achieving an average performance of approximately 1 second per frame. This demonstrates that the proposed framework efficiently supports high-resolution, geometry-rich fluid–solid simulations while preserving rich small-scale flow details.

6.5 Real-time Simulations

We demonstrate real-time smoke simulations interacting with solids that exhibit highly complex porous microgeometry. The dense, irregular fluid–solid interfaces generate intense multi-scale turbulence while simultaneously imposing stringent stability and performance demands on the solver. Despite these challenges, our method remains numerically stable and consistently sustains real-time performance across all tested porous configurations.

Table 1. Experimental and Timing Statistics. Per-iteration timings are reported in milliseconds, while total time is reported in seconds and corresponds to the accumulated time of the entire simulation (all iterations).

Fig.	Resolution	# Faces	fluid	buffer	solid	#iters	total
			update (ms)	copy (ms)	correction (ms)		
1	$1000 \times 400 \times 400$	2268848	17.7	10.8	7.6	9000	324.9
2	$1000 \times 400 \times 400$	5329024	17.7	10.8	12.4	9000	368.1
3	$1024 \times 1024 \times 1024$	-	151.3	-	-	8100	1225.5
4 (lod1)	$256 \times 512 \times 256$	15360	3.1	2.2	0.2	6750	36.9
4 (lod2)	$256 \times 512 \times 256$	37632	3.1	2.2	0.3	6750	37.8
4 (lod3)	$256 \times 512 \times 256$	70720	3.1	2.2	0.6	6750	39.8
4 (lod4)	$256 \times 512 \times 256$	145432	3.1	2.2	1.3	6750	44.5
6 (a)	$720 \times 360 \times 360$	188672	10.1	6.3	0.8	7500	129.0
6 (b)	$720 \times 360 \times 360$	754688	10.1	6.3	2.1	7500	138.8
6 (c)	$720 \times 360 \times 360$	754688	9.1	6.1	2.6	7500	133.5
7	$660 \times 250 \times 330$	240000	5.3	3.4	0.4	9000	81.9
13	$512 \times 256 \times 256$	1280	3.2	2.2	0.05	6000	32.7
11 (a)	$256 \times 128 \times 128$	128996	0.4	0.3	0.39	4500	4.9
11 (b)	$256 \times 128 \times 128$	129000	0.4	0.3	0.35	4500	4.7
11 (c)	$256 \times 128 \times 128$	238394	0.4	0.3	0.66	4500	6.1
11 (d)	$256 \times 128 \times 128$	30720	0.4	0.3	0.16	4500	3.9
12	$256 \times 128 \times 128$	8	0.4	0.3	0.01	4500	3.2

7 Conclusion

We presented a stability-guided GPU framework for memory-efficient, high-performance moment-based lattice Boltzmann simulation with complex fluid–solid interaction. A decoupled split-kernel design reduces warp divergence and

improves GPU utilization, while a von Neumann stability analysis yields moment-wise bounds that enable robust 16-bit quantization. Together, these techniques significantly reduce memory footprint without sacrificing numerical stability. Our experiments demonstrate substantial memory savings and up to an order-of-magnitude speedup over representative baselines, enabling higher-resolution simulations within the constraints of a single GPU while running at a few seconds per frame. More broadly, this work illustrates how theoretical stability analysis can directly inform practical system design for scalable LBM simulation.

Limitations and future work. Our current implementation assumes single-layer surface meshes and does not yet support thin shells, layered geometry, or complex self-intersections, which would require more advanced inside–outside classification and intersection handling. Moreover, while our boundary treatment is optimized for robustness and throughput, we do not explicitly evaluate sub-cell geometric accuracy or boundary error convergence; incorporating wall-function models [Liu et al. 2025] is a promising direction. A 3D von Neumann stability analysis for HOME-LBM would be a valuable addition, providing a more complete assessment of its stability properties. Several promising directions remain for future research, such as extending the framework to moving solids and fully coupled two-way interactions, as well as integrating multi-resolution or adaptive discretization to further improve scalability for large-scale scenes.

References

Nadir Akinci, Markus Ihmsen, Gizem Akinci, Barbara Solenthaler, and Matthias Teschner. 2012. Versatile rigid-fluid coupling for incompressible SPH. *ACM Trans. Graph.* 31, 4, Article 62 (July 2012), 8 pages.

Prabhu Lal Bhathnagar, Eugene P. Gross, and Max Krook. 1954. A model for collision processes in gases. *Physical Review* 94, 3 (1954), 511.

M Chávez-Modena, E Ferrer, and G Rubio. 2018. Improving the stability of multiple-relaxation lattice Boltzmann methods with central moments. *Computers & Fluids* 172 (2018), 397–409.

Shiyi Chen and Gary D Doolen. 1998. Lattice Boltzmann method for fluid flows. *Annual Review of Fluid Mechanics* 30, 1 (1998), 329–364.

Yixin Chen, David Levin, and Timothy Langlois. 2024. Fluid Control with Laplacian Eigenfunctions. In *ACM SIGGRAPH 2024 Conference Papers* (Denver, CO, USA) (SIGGRAPH '24). Association for Computing Machinery, New York, NY, USA, Article 44, 11 pages.

Yixin Chen, Wei Li, Rui Fan, and Xiaopei Liu. 2022. GPU Optimization for High-Quality Kinetic Fluid Simulation. *IEEE Transactions on Visualization and Computer Graphics* 28, 9 (2022), 3235–3251.

Zhili Chen, Byungmoon Kim, Daichi Ito, and Huamin Wang. 2015. Wetbrush: GPU-based 3D Painting Simulation at the Bristle Level. *ACM Trans. Graph.* 34, 6, Article 200 (Oct. 2015), 11 pages.

Nuttapong Chentanez and Matthias Müller. 2011. Real-time Eulerian Water Simulation Using a Restricted Tall Cell Grid. *ACM Trans. Graph.* 30, 4, Article 82 (July 2011), 10 pages.

Christophe Coreixas, Gauthier Wissocq, Guillaume Puigt, Jean-François Boussuge, and Pierre Sagaut. 2017. Recursive regularization step for high-order lattice Boltzmann methods. *Phys. Rev. E* 96 (Sep 2017), 033306. Issue 3.

Alessandro De Rosis. 2017. Nonorthogonal central-moments-based lattice Boltzmann scheme in three dimensions. *Phys. Rev. E* 95 (Jan 2017), 013310. Issue 1.

Alessandro De Rosis and Kai H. Luo. 2019. Role of higher-order Hermite polynomials in the central-moments-based lattice Boltzmann framework. *Phys. Rev. E* 99 (Jan 2019), 013301. Issue 1.

Jean M Délery. 2001. Robert Legendre and Henri Werlé: toward the elucidation of three-dimensional separation. *Annual review of fluid mechanics* 33, 1 (2001), 129–154.

Yitong Deng, Hong-Xing Yu, Diyang Zhang, Jiajun Wu, and Bo Zhu. 2023. Fluid Simulation on Neural Flow Maps. *ACM Trans. Graph.* 42, 6, Article 248 (Dec. 2023), 21 pages.

Dominique d’Humières. 1992. Generalized lattice-Boltzmann equations. *Rarefied gas dynamics* (1992).

Tao Du, Kui Wu, Andrew Spielberg, Wojciech Matusik, Bo Zhu, and Eftychios Sifakis. 2020. Functional optimization of fluidic devices with differentiable stokes flow. *ACM Trans. Graph.* 39, 6, Article 197 (Nov. 2020), 15 pages.

François Dubois, Tony Février, and Benjamin Graille. 2015. On the stability of a relative velocity lattice Boltzmann scheme for compressible Navier–Stokes equations. *Comptes Rendus. Mécanique* 343, 10-11 (2015), 599–610.

Chuyuan Fu, Qi Guo, Theodore Gast, Chenfanfu Jiang, and Joseph Teran. 2017. A polynomial particle-in-cell method. *ACM Trans. Graph.* 36, 6, Article 222 (Nov. 2017), 12 pages.

Ming Gao, Xinlei Wang, Kui Wu, Andre Pradhana, Eftychios Sifakis, Cem Yuksel, and Chenfanfu Jiang. 2018. GPU optimization of material point methods. *ACM Transactions on Graphics (TOG)* 37, 6 (2018), 1–12.

Martin Geier, Andreas Greiner, and Jan G. Korvink. 2006. Cascaded digital lattice Boltzmann automata for high Reynolds number flow. *Phys. Rev. E* 73 (Jun 2006), 066705. Issue 6.

Stewart Harris. 2004. *An introduction to the theory of the Boltzmann equation*. Courier Corporation.

F J Higuera and Javier Jiménez. 1989. Boltzmann approach to lattice gas simulations. *Europhysics letters* 9, 7 (1989), 663.

Christopher Horvath and Willi Geiger. 2009. Directable, High-resolution Simulation of Fire on the GPU. *ACM Trans. Graph.* 28, 3, Article 41 (July 2009), 8 pages.

Changyu Hu, Yanke Qu, Qiuhan Yang, Xiaoyu Xiong, Wei Kui Wu, Li, and Tao Du. 2025. Learning to Control Free-Form Soft Swimmers. In *The Thirty-ninth Annual Conference on Neural Information Processing Systems*. Curran Associates, Inc., NY, United States, 19 pages. <https://openreview.net/forum?id=Z01gNs09SW>

Yuanming Hu, Jiafeng Liu, Xuanda Yang, Mingkuan Xu, Ye Kuang, Weiwei Xu, Qiang Dai, William T. Freeman, and Frédéric Durand. 2021. QuanTaichi: a compiler for quantized simulations. *ACM Trans. Graph.* 40, 4, Article 182 (July 2021), 16 pages.

Chenfanfu Jiang, Craig Schroeder, Andrew Selle, Joseph Teran, and Alexey Stomakhin. 2015. The affine particle-in-cell method. *ACM Trans. Graph.* 34, 4, Article 51 (July 2015), 10 pages.

M. Jovanovic and B. Bamieh. 2001. Modeling flow statistics using the linearized Navier-Stokes equations. In *Proceedings of the 40th IEEE Conference on Decision and Control (Cat. No.01CH37228)*, Vol. 5. 4944–4949 vol.5.

ByungMoon Kim, Yingjie Liu, Ignacio LLamas, and Jarek Rossignac. 2005. FlowFixer: using BFECC for fluid simulation. In *Proceedings of the First Eurographics Conference on Natural Phenomena* (Dublin, Ireland) (NPH'05). Eurographics Association, Goslar, DEU, 51–56.

Doyub Kim, Minjae Lee, and Ken Museth. 2024. Neuralvdb: High-resolution sparse volume representation using hierarchical neural networks. *ACM Transactions on Graphics* 43, 2 (2024), 1–21.

Anthony J. C. Ladd. 1994. Numerical simulations of particulate suspensions via a discretized Boltzmann equation. Part 1. Theoretical foundation. *Journal of Fluid Mechanics* 271 (1994), 285–309.

Pierre Lallemand and Li-Shi Luo. 2000. Theory of the lattice Boltzmann method: Dispersion, dissipation, isotropy, Galilean invariance, and stability. *Physical review E* 61, 6 (2000), 6546.

Moritz Lehmann. 2022. Esoteric pull and esoteric push: two simple in-place streaming schemes for the lattice Boltzmann method on GPUs. *Computation* 10, 6 (2022), 92.

Wei Li, Yixin Chen, Mathieu Desbrun, Changxi Zheng, and Xiaopei Liu. 2020. Fast and scalable turbulent flow simulation with two-way coupling. *ACM Trans. Graph.* 39, 4, Article 47 (Aug. 2020), 20 pages.

Wei Li and Mathieu Desbrun. 2023. Fluid-Solid Coupling in Kinetic Two-Phase Flow Simulation. *ACM Trans. Graph.* 42, 4, Article 123 (July 2023), 14 pages.

Wei Li, Daoming Liu, Mathieu Desbrun, Jin Huang, and Xiaopei Liu. 2021. Kinetic-Based Multiphase Flow Simulation. *IEEE Trans. Vis. Comp. Graph.* 27, 7 (2021), 3318–3334.

Wei Li, Yihui Ma, Xiaopei Liu, and Mathieu Desbrun. 2022b. Efficient kinetic simulation of two-phase flows. *ACM Trans. Graph.* 41, 4, Article 114 (July 2022), 17 pages.

Wei Li, Tongtong Wang, Zherong Pan, Xifeng Gao, Kui Wu, and Mathieu Desbrun. 2023. High-order moment-encoded kinetic simulation of turbulent flows. *ACM Transactions on Graphics (TOG)* 42, 6 (2023), 1–13.

Wei Li, Xiaoming Wei, and Arie Kaufman. 2003. Implementing lattice Boltzmann computation on graphics hardware. *Vis. Comput.* 19, 7–8 (Dec. 2003), 444–456.

Yifei Li, Tao Du, Sangeetha Grama Srinivasan, Kui Wu, Bo Zhu, Eftychios Sifakis, and Wojciech Matusik. 2022a. Fluidic Topology Optimization with an Anisotropic Mixture Model. *ACM Trans. Graph.* 41, 6, Article 239 (Nov. 2022), 14 pages.

Jiafeng Liu, Haoyang Shi, Siyuan Zhang, Yin Yang, Chongyang Ma, and Weiwei Xu. 2022b. Automatic quantization for physics-based simulation. *ACM Trans. Graph.* 41, 4, Article 51 (July 2022), 16 pages.

Mengyun Liu, Kai Bai, and Xiaopei Liu. 2025. A Hybrid Near-wall Model for Kinetic Simulation of Turbulent Boundary Layer Flows. *ACM Transactions on Graphics (TOG)* 44, 4 (2025), 1–24.

Mengyun Liu and Xiaopei Liu. 2023. A Parametric Kinetic Solver for Simulating Boundary-Dominated Turbulent Flow Phenomena. *ACM Trans. Graph.* 42, 6, Article 189 (Dec. 2023), 20 pages.

Wenji Liu, Kai Bai, Xuming He, Shuran Song, Changxi Zheng, and Xiaopei Liu. 2022a. FishGym: A High-Performance Physics-based Simulation Framework for Underwater Robot Learning. In *2022 International Conference on Robotics and Automation (ICRA)*. IEEE Press, Philadelphia, PA, USA, 6268–6275.

Chaoyang Lyu, Kai Bai, Yiheng Wu, Mathieu Desbrun, Changxi Zheng, and Xiaopei Liu. 2023. Building a Virtual Weakly-Compressible Wind Tunnel Testing Facility. *ACM Trans. Graph.* 42, 4, Article 125 (July 2023), 20 pages.

Chaoyang Lyu, Wei Li, Mathieu Desbrun, and Xiaopei Liu. 2021. Fast and versatile fluid-solid coupling for turbulent flow simulation. *ACM Trans. Graph.* 40, 6, Article 201 (Dec. 2021), 18 pages.

Pingchuan Ma, Tao Du, John Z. Zhang, Kui Wu, Andrew Spielberg, Robert K. Katzschnann, and Wojciech Matusik. 2021. DiffAqua: a differentiable computational design pipeline for soft underwater swimmers with shape interpolation. *ACM Trans. Graph.* 40, 4, Article 132 (July 2021), 14 pages.

Pingchuan Ma, Yunsheng Tian, Zherong Pan, Bo Ren, and Dinesh Manocha. 2018. Fluid directed rigid body control using deep reinforcement learning. *ACM Trans. Graph.* 37, 4, Article 96 (July 2018), 11 pages.

Orestis Malaspinas. 2015. Increasing stability and accuracy of the lattice Boltzmann scheme: recursivity and regularization. arXiv:1505.06900 [physics.flu-dyn]

Julien N. P. Martel, David B. Lindell, Connor Z. Lin, Eric R. Chan, Marco Monteiro, and Gordon Wetzstein. 2021. Acorn: adaptive coordinate networks for neural scene representation. *ACM Trans. Graph.* 40, 4, Article 58 (July 2021), 13 pages.

Maxon. 2026. The world's first fully GPU-accelerated, biased renderer. <https://www.maxon.net/en/redshift>.

Ken Museth, Jeff Budsberg, Alexandre Sirois-Vigneux, Gregory Hurst, Francis Williams, Andre Pradhana, Dan Bailey, and Nick Avramoussis. 2025. OpenVDB. In *Proceedings of the Special Interest Group on Computer Graphics and Interactive Techniques Conference Courses (SIGGRAPH Courses '25)*. Association for Computing Machinery, New York, NY, USA, Article 1, 4 pages.

Mohammad Sina Nabizadeh, Ritoban Roy-Chowdhury, Hang Yin, Ravi Ramamoorthi, and Albert Chern. 2024. Fluid Implicit Particles on Coadjoint Orbits. *ACM Trans. Graph.* 43, 6, Article 270 (Nov. 2024), 38 pages.

Mohammad Sina Nabizadeh, Stephanie Wang, Ravi Ramamoorthi, and Albert Chern. 2022. Covector fluids. *ACM Transactions on Graphics (TOG)* 41, 4 (2022), 1–16.

Andreas Peer, Markus Ihmsen, Jens Cornelis, and Matthias Teschner. 2015. An implicit viscosity formulation for SPH fluids. *ACM Trans. Graph.* 34, 4, Article 114 (July 2015), 10 pages.

Charles S Peskin. 1972. Flow patterns around heart valves: a numerical method. *J. Comput. Phys.* 10, 2 (1972), 252–271.

Tobias Pfaff, Nils Thuerey, and Markus Gross. 2012. Lagrangian vortex sheets for animating fluids. *ACM Trans. Graph.* 31, 4, Article 112 (July 2012), 8 pages.

Ziyin Qu, Xinxin Zhang, Ming Gao, Chenfanfu Jiang, and Baoquan Chen. 2019. Efficient and conservative fluids using bidirectional mapping. *ACM Trans. Graph.* 38, 4, Article 128 (July 2019), 12 pages.

Amir Hossein Rabbani, Jean-Philippe Guertin, Damien Rioux-Lavoie, Arnaud Schoentgen, Kaitai Tong, Alexandre Sirois-Vigneux, and Derek Nowrouzezahrai. 2022. Compact Poisson Filters for Fast Fluid Simulation. In *ACM SIGGRAPH 2022 Conference Proceedings* (Vancouver, BC, Canada) (SIGGRAPH '22). Association for Computing Machinery, New York, NY, USA, Article 35, 9 pages.

P.R. Rinaldi, E.A. Dari, M.J. Vénere, and A. Clausse. 2012. A Lattice-Boltzmann solver for 3D fluid simulation on GPU. *Simulation Modelling Practice and Theory* 25 (2012), 163–171.

Andrew Selle, Ronald Fedkiw, Byungmoon Kim, Yingjie Liu, and Jarek Rossignac. 2008. An Unconditionally Stable MacCormack Method. *J. Sci. Comput.* 35, 2–3 (June 2008), 350–371.

Andrew Selle, Nick Rasmussen, and Ronald Fedkiw. 2005. A vortex particle method for smoke, water and explosions. In *ACM SIGGRAPH 2005 Papers* (Los Angeles, California) (SIGGRAPH '05). Association for Computing Machinery, New York, NY, USA, 910–914.

Xiaowen Shan, Xue-Feng Yuan, and Hudong Chen. 2006. Kinetic theory representation of hydrodynamics: a way beyond the Navier–Stokes equation. *J. Fluid Mech.* 550 (2006), 413–441.

DN Siebert, LA Hegele Jr, and Paulo C Philippi. 2008. Lattice Boltzmann equation linear stability analysis: Thermal and athermal models. *Physical Review E–Statistical, Nonlinear, and Soft Matter Physics* 77, 2 (2008), 026707.

B. Solenthaler and R. Pajarola. 2009. Predictive-corrective incompressible SPH. *ACM Trans. Graph.* 28, 3, Article 40 (July 2009), 6 pages.

Wenbin Song, Heng Zhang, Yang Wang, and Xiaopei Liu. 2025. Creating Fluid-Interactive Virtual Agents by an Efficient Simulator with Local-domain Control. *ACM Trans. Graph.* 44, 4, Article 103 (July 2025), 19 pages.

Jos Stam. 1999. Stable fluids. In *Proceedings of the 26th Annual Conference on Computer Graphics and Interactive Techniques (SIGGRAPH '99)*. ACM Press/Addison-Wesley Publishing Co., USA, 121–128.

James D Sterling and Shiyi Chen. 1996. Stability analysis of lattice Boltzmann methods. *J. Comput. Phys.* 123, 1 (1996), 196–206.

Yuchen Sun, Junlin Li, Ruicheng Wang, Sinan Wang, Zhiqi Li, Bart G. van Bloemen Waanders, and Bo Zhu. 2025. Leapfrog Flow Maps for Real-Time Fluid Simulation. *ACM Trans. Graph.* 44, 4, Article 94 (July 2025), 12 pages.

Niels Thürey and Ulrich Rüde. 2009. Stable free surface flows with the lattice Boltzmann method on adaptively coarsened grids. *Comput. Visual Sci.* 12 (2009), 247–263.

J. Von Neumann and R. D. Richtmyer. 1950. A Method for the Numerical Calculation of Hydrodynamic Shocks. *Journal of Applied Physics* 21, 3 (03 1950), 232–237.

Haoxiang Wang, Kui Wu, Hui Qiao, Mattieu Desbrun, and Wei Li. 2025. Kinetic Free-Surface Flows and Foams with Sharp Interfaces. *ACM Trans. Graph.* 44, 6, Article 266 (Nov. 2025), 17 pages.

Sinan Wang, Yitong Deng, Molin Deng, Hong-Xing Yu, Junwei Zhou, Duowen Chen, Taku Komura, Jiajun Wu, and Bo Zhu. 2024. An eulerian vortex method on flow maps. *ACM Transactions on Graphics (TOG)* 43, 6 (2024), 1–14.

Xinlei Wang, Yuxing Qiu, Stuart R. Slattery, Yu Fang, Minchen Li, Song-Chun Zhu, Yixin Zhu, Min Tang, Dinesh Manocha, and Chenfanfu Jiang. 2020. A massively parallel and scalable multi-GPU material point method. *ACM Trans. Graph.* 39, 4, Article 30 (Aug. 2020), 15 pages.

Steffen Weismann and Ulrich Pinkall. 2010. Filament-based smoke with vortex shedding and variational reconnection. *ACM Trans. Graph.* 29, 4, Article 115 (July 2010), 12 pages.

Gauthier Wissocq, Christophe Coreixas, and Jean-François Boussuge. 2020. Linear stability and isotropy properties of athermal regularized lattice Boltzmann methods. *Physical Review E* 102, 5 (2020), 053305.

Zhou Xian, Bo Zhu, Zhenjia Xu, Hsiao-Yu Tung, Antonio Torralba, Katerina Fragkiadaki, and Chuang Gan. 2023. FluidLab: A Differentiable Environment for Benchmarking Complex Fluid Manipulation. In *International Conference on Learning Representations*. Curran Associates, Inc., WI, United States,

19 pages.

Jonas Zehnder, Rahul Narain, and Bernhard Thomaszewski. 2018. An advection-reflection solver for detail-preserving fluid simulation. *ACM Trans. Graph.* 37, 4, Article 85 (July 2018), 8 pages.

Xinxin Zhang, Robert Bridson, and Chen Greif. 2015. Restoring the missing vorticity in advection-projection fluid solvers. *ACM Trans. Graph.* 34, 4, Article 52 (July 2015), 8 pages.

Xinxin Zhang, Minchen Li, and Robert Bridson. 2016. Resolving fluid boundary layers with particle strength exchange and weak adaptivity. *ACM Trans. Graph.* 35, 4, Article 76 (July 2016), 8 pages.

A HOME-LBM Collision Operator

The high-order moment-space collision operator updates the velocity moments directly as follows:

$$\rho(\mathbf{x}, t + 1) = \rho^*, \quad (33)$$

$$u_\alpha(\mathbf{x}, t + 1) = u_\alpha^* + F_\alpha/(2\rho^*), \quad (34)$$

$$S_{\alpha\beta}(\mathbf{x}, t + 1) = (1 - 1/\tau)S_{\alpha\beta}^* + \frac{1}{\tau}u_\alpha^*u_\beta^* + \frac{2\tau - 1}{2\tau\rho^*}(F_\alpha u_\beta^* + F_\beta u_\alpha^*), \quad (35)$$

$$\begin{aligned} S_{\alpha\alpha}(\mathbf{x}, t + 1) = & \frac{\tau - 1}{3\tau}(2S_{\alpha\alpha}^* - S_{\beta\beta}^* - S_{\gamma\gamma}^*) + \frac{1}{3}(u_\alpha^{*2} + u_\beta^{*2} + u_\gamma^{*2}) \\ & + \frac{1}{3\tau}(2u_\alpha^{*2} - u_\beta^{*2} - u_\gamma^{*2}) + \frac{1}{\rho^*}F_\alpha u_\alpha^* \\ & + \frac{\tau - 1}{3\tau\rho^*}(2F_\alpha u_\alpha^* - F_\beta u_\beta^* - F_\gamma u_\gamma^*). \end{aligned} \quad (36)$$

All symbols are defined in Sec. 3.

B Amplification matrices of Different Collision Models

For different collision models (BGK [Bhathnagar et al. 1954], NOCM-MRT [De Rosis and Luo 2019]) in LBM, the corresponding amplification matrices \mathbf{G}_{ij} can be obtained, written as [Chávez-Modena et al. 2018]:

$$\begin{aligned} \mathbf{G}_{ij}^{\text{BGK}} &= e^{-i\mathbf{k}\cdot\mathbf{c}_i} \left[\mathbf{I} - \frac{1}{\tau}(\mathbf{I} - \mathbf{\Lambda}) \right]_{ij}, \\ \mathbf{G}_{ij}^{\text{NOCM-MRT}} &= e^{-i\mathbf{k}\cdot\mathbf{c}_i} \left[\mathbf{I} - \mathbf{M}^{-1}\mathbf{R}\mathbf{M}(\mathbf{I} - \mathbf{\Lambda}) \right]_{ij}. \end{aligned} \quad (37)$$

where \mathbf{M} is the projection matrix in NOCM-MRT collision model whose definition can be found in [Li et al. 2020] and where \mathbf{R} is a diagonal matrix whose values are relaxation rates $\{r_i\}_{i=1\dots q}$.

C Collision Models

Collision modeling plays a central role in determining both the accuracy and the stability of lattice Boltzmann solvers. In this appendix, we provide the complete 2D mathematical formulations of the collision models referenced in the main text, including explicit equations, full operator definitions, and implementation-ready expressions. This appendix is organized to progress from the classical single-relaxation-time BGK model to the raw-moment multiple-relaxation-time (RM-MRT) model and the non-orthogonal central-moment multiple-relaxation-time (NOCM-MRT) model, and finally to the moment-encoded NOCM-MRT collision scheme adopted in HOME-LBM.

C.1 Single Relaxation Time BGK model

The classical Bhatnagar-Gross-Krook (BGK) formulation applies a single relaxation time to relax each lattice population toward its local equilibrium. The collision operator is written as

$$\Omega_i^{\text{BGK}} = -\frac{1}{\tau} (f_i - f_i^{\text{eq}}), \quad (38)$$

where τ is the relaxation time determining the rate at which the distribution function approaches equilibrium. The BGK model yields the following relations between $\tau = \frac{1}{3v+0.5}$, where v is the kinematic viscosity.

C.2 Raw Moment Multiple Relaxation Time (RM-MRT) Model

To overcome the stability limitations of the BGK approximation, the MRT framework introduces a more stable collision operator that acts in moment space rather than directly on the distribution functions [Chávez-Modena et al. 2018]. In the RM-MRT formulation, the collision model is performed on polynomial moments constructed from the lattice velocities. Let $\mathbf{M}(0)$ denote the raw-moment transformation matrix, which is independent of the local fluid velocity. The moment vector is obtained by:

$$\mathbf{m} = \mathbf{M}(0) \mathbf{f}, \quad \mathbf{m}^{\text{eq}} = \mathbf{M}(0) \mathbf{f}^{\text{eq}}, \quad (39)$$

where \mathbf{f} is the vector of populations $\{f_i\}$ and \mathbf{m}^{eq} denotes the raw-moment equilibrium. The RM-MRT collision operator is then expressed as

$$\Omega_i^{\text{RM}} = -\mathbf{M}(0)^{-1} \mathbf{R} (m_i - m_i^{\text{eq}}) \quad (40)$$

$$= -\mathbf{M}(0)^{-1} \mathbf{R} \mathbf{M}(0) (f_i - f_i^{\text{eq}}) \quad (41)$$

where

$$\mathbf{R} = \text{diag}(r_0, r_1, \dots, r_8), \quad (42)$$

is a diagonal matrix of relaxation rates for each moment.

C.3 Non-Orthogonal Central Moment Multiple Relaxation time (NOCM-MRT) Model

While MRT-RM improves stability compared to BGK, its use of raw moments lacks Galilean invariance, which can lead to degraded accuracy and instabilities at low viscosities. Non-orthogonal central moment multiple relaxation time model (NOCM-MRT) addresses this issue by defining moments relative to the local fluid velocity, thereby achieving significantly improved invariance properties and enhanced robustness and accuracy for turbulent flows [De Rosis and Luo 2019].

Let \mathbf{u} denote the local macroscopic velocity, and let $\mathbf{M}(\mathbf{u})$ be the central-moment transformation matrix, which shifts the velocity basis so that the resulting moments are computed with respect to $\mathbf{c}_i - \mathbf{u}$. The central moments are defined as:

$$\mathbf{m} = \mathbf{M}(\mathbf{u}) \mathbf{f}, \quad \mathbf{m}^{\text{eq}} = \mathbf{M}(\mathbf{u}) \mathbf{f}^{\text{eq}}, \quad (43)$$

where \mathbf{m}^{eq} represents the central-moment equilibrium obtained from the Maxwellian equilibrium distribution. The NOCM-MRT collision operator is then expressed as

$$\Omega_i^{\text{CM}} = -\mathbf{M}(\mathbf{u})^{-1} \mathbf{R} (m_i - m_i^{\text{eq}}) \quad (44)$$

$$= -\mathbf{M}(\mathbf{u})^{-1} \mathbf{R} \mathbf{M}(\mathbf{u}) (f_i - f_i^{\text{eq}}) \quad (45)$$

where R is a diagonal relaxation matrix specifying independent relaxation rates for each central moment. Relaxing higher-order moments more aggressively provide strong damping of non-hydrodynamic modes while preserving the correct recovery of Navier-Stokes dynamics [Li et al. 2020].

C.4 D2Q9 Implementation Details

C.4.1 D2Q9 Lattice Definitions. For completeness, we list the discrete velocities, lattice weights, and the lattice speed of sound used throughout this work. The D2Q9 lattice consists of nine discrete velocity directions

$$\mathbf{c}_i = (c_{x,i}, c_{y,i}), \quad i = 0, \dots, 8,$$

with components:

$$\begin{aligned} c_x &= \begin{pmatrix} 0 & 1 & 0 & -1 & 0 & 1 & -1 & -1 & 1 \end{pmatrix} \\ c_y &= \begin{pmatrix} 0 & 0 & 1 & 0 & -1 & 1 & 1 & -1 & -1 \end{pmatrix}. \end{aligned}$$

The corresponding lattice weights are

$$\mathbf{w} = \left(\frac{4}{9}, \frac{1}{9}, \frac{1}{9}, \frac{1}{9}, \frac{1}{9}, \frac{1}{36}, \frac{1}{36}, \frac{1}{36}, \frac{1}{36} \right).$$

The lattice speed of sound is $c_s = \sqrt{\frac{1}{3}}$. Above definitions are used for constructing the MRT-RM matrix \mathbf{M}^{RM} , the NOCM-MRT transformation matrix $\mathbf{M}^{\text{NOCM}}(\mathbf{u})$, and all Hermite-based reconstructions described in this appendix.

C.4.2 RM-MRT Transformation Matrix. For the D2Q9 lattice with discrete velocities $(c_{x,i}, c_{y,i})_{i=0}^8$, transformation matrix \mathbf{M}^{RM} used in Eq. (41) is

$$\mathbf{M}^{\text{RM}} = \begin{pmatrix} 1 & 1 & 1 & 1 & 1 & 1 & 1 & 1 & 1 \\ 0 & 1 & 0 & -1 & 0 & 1 & -1 & -1 & 1 \\ 0 & 0 & 1 & 0 & -1 & 1 & 1 & -1 & -1 \\ 0 & 1 & 1 & 1 & 1 & 2 & 2 & 2 & 2 \\ 0 & 1 & -1 & 1 & -1 & 0 & 0 & 0 & 0 \\ 0 & 0 & 0 & 0 & 0 & 1 & -1 & 1 & -1 \\ 0 & 1 & 0 & -1 & 0 & 2 & -2 & -2 & 2 \\ 0 & 0 & 1 & 0 & -1 & 2 & 2 & -2 & -2 \\ 0 & 0 & 0 & 0 & 0 & 1 & 1 & 1 & 1 \end{pmatrix}.$$

C.4.3 NOCM-MRT Transformation Matrix. Let the shifted velocities be

$$X_i = c_{x,i} - u_x, \quad Y_i = c_{y,i} - u_y.$$

The transformation matrix $M^{\text{NOCM}}(\mathbf{u})$ is then

$$M^{\text{NOCM}}(\mathbf{u}) = \begin{pmatrix} 1 \\ X_i \\ Y_i \\ X_i^2 + Y_i^2 \\ X_i^2 - Y_i^2 \\ X_i Y_i \\ X_i^2 Y_i \\ X_i Y_i^2 \\ X_i^2 Y_i^2 \end{pmatrix} = \begin{pmatrix} 1 & 1 & \cdots & 1 \\ X_0 & X_1 & \cdots & X_8 \\ Y_0 & Y_1 & \cdots & Y_8 \\ X_0^2 + Y_0^2 & X_1^2 + Y_1^2 & \cdots & X_8^2 + Y_8^2 \\ X_0^2 - Y_0^2 & X_1^2 - Y_1^2 & \cdots & X_8^2 - Y_8^2 \\ X_0 Y_0 & X_1 Y_1 & \cdots & X_8 Y_8 \\ X_0^2 Y_0 & X_1^2 Y_1 & \cdots & X_8^2 Y_8 \\ X_0 Y_0^2 & X_1 Y_1^2 & \cdots & X_8 Y_8^2 \\ X_0^2 Y_0^2 & X_1^2 Y_1^2 & \cdots & X_8^2 Y_8^2 \end{pmatrix}.$$

C.4.4 Matrix Inversion in RM-MRT and NOCM-MRT. Both the RM- and NOCM-MRT formulations require the inverse of the moment transformation matrix during the collision step. In numerical implementations, the matrix inverse is evaluated directly by $M^{-1} = \text{np.linalg.inv}(M)$, which is feasible due to the small fixed size (9×9 in the D2Q9 lattice).

C.4.5 Relaxation Rates. The relaxation rates for the MRT-RM model are collected in the vector

$$\mathbf{r}^{\text{RM}} = \left(0, 0, 0, 1.64, r_\nu, r_\nu, 1.9, 1.9, 1.54 \right)^\top,$$

where $r_\nu = \frac{1}{0.5 + \nu/c_s^2}$. Similarly, the relaxation rate matrix for the NOCM-MRT model

$$\mathbf{r}^{\text{NOCM}} = \left(0, 0, 0, s_\nu, s_\nu, s_\nu, 1.0, 1.0, 1.0 \right)^\top$$

The diagonal relaxation matrix is then constructed as

$$\mathbf{R} = \text{diag}(\mathbf{r}),$$

where the operator $\text{diag}(\cdot)$ places the components of the vector on the main diagonal of the matrix.

D Matrix Definition

D.1 Recursive Matrices

In component form:

$$a_{1,\alpha\alpha}^{(2)} = \rho(S_{\alpha\alpha} - u_\alpha^2), \quad a_{1,\alpha\beta}^{(2)} = \rho(S_{\alpha\beta} - u_\alpha u_\beta). \quad (46)$$

In the recursive regularization procedure, the non-equilibrium third-order coefficients $a_1^{(3)}$ are obtained recursively from non-equilibrium $a_1^{(2)}$ and the local velocity u_α . The recursion is given by:

$$a_{1,\alpha\alpha\alpha}^{(3)} = 3 u_\alpha a_{1,\alpha\alpha}^{(2)}, \quad a_{1,\alpha\alpha\beta}^{(3)} = 2 u_\alpha a_{1,\alpha\beta}^{(2)} + u_\beta a_{1,\alpha\alpha}^{(2)}, \quad (47)$$

where repeated indices are not summed unless explicitly stated.

The non-equilibrium distribution function f_i^{neq} is reconstructed from these quantities in Hermite space as

$$f_i^{\text{neq}} = w_i \left[\frac{1}{2c_s^4} H_i^{(2)} : a_1^{(2)} + \frac{1}{2c_s^6} \left(H_{i,xx}^{(3)} a_{1,xx}^{(3)} + H_{i,xy}^{(3)} a_{1,xy}^{(3)} \right) \right], \quad (48)$$

where for the D2Q9 lattice, the second- and third-order Hermite tensors are

$$\begin{aligned} H_{i,\alpha\beta}^{(2)} &= c_{i\alpha}c_{i\beta} - c_s^2\delta_{\alpha\beta}, \\ H_{i,xx}^{(3)} &= c_{iy}(c_{ix}^2 - c_s^2), \\ H_{i,xy}^{(3)} &= c_{ix}(c_{iy}^2 - c_s^2). \end{aligned} \quad (49)$$

Collecting all populations into the vector and grouping the Hermite coefficients into $\mathbf{a}_1^{(2)} \in \mathbb{R}^{3 \times 1}$ and $\mathbf{a}_1^{(3)} \in \mathbb{R}^{4 \times 1}$, the above expression can be written as

$$\mathbf{f}^{neq} = \mathbf{A}_2 \mathbf{a}_1^{(2)} + \mathbf{A}_3 \mathbf{a}_1^{(3)}, \quad (50)$$

where $\mathbf{A}_2 \in \mathbb{R}^{9 \times 3}$ and $\mathbf{A}_3 \in \mathbb{R}^{9 \times 4}$ collect the discrete Hermite basis contributions:

$$(\mathbf{A}_2)_{i,:} = \frac{w_i}{2c_s^4} \begin{bmatrix} c_{ix}^2 - c_s^2 & c_{ix}c_{iy} & c_{iy}^2 - c_s^2 \end{bmatrix}, \quad (51)$$

$$(\mathbf{A}_3)_{i,:} = \frac{w_i}{6c_s^6} \begin{bmatrix} c_{ix}^3 - 3c_s^2c_{ix} & c_{ix}^2c_{iy} - c_s^2c_{iy} \\ c_{ix}c_{iy}^2 - c_s^2c_{ix} & c_{iy}^3 - 3c_s^2c_{iy} \end{bmatrix}. \quad (52)$$

Using the recursive relation $\mathbf{a}_1^{(3)} = \mathbf{R}_u \mathbf{a}_1^{(2)}$, with

$$\mathbf{R}_u = \begin{bmatrix} 3u_x & 0 & 0 \\ u_y & 2u_x & 0 \\ 0 & 2u_y & u_x \\ 0 & 0 & 3u_y \end{bmatrix},$$

D.2 Explicit Form of the Matrix B for D2Q9

We define the deviatoric second-order moment vector in Voigt form as

$$\mathbf{S}^* = \begin{bmatrix} S_{xx}^* \\ 2S_{xy}^* \\ S_{yy}^* \end{bmatrix}, \quad S_{\alpha\beta}^* = \sum_i f_i (c_{i\alpha}c_{i\beta} - c_s^2\delta_{\alpha\beta}), \quad (53)$$

where c_s denotes the lattice sound speed. The linear mapping from the distribution function vector \mathbf{f} to \mathbf{S}^* is written as

$$\mathbf{S}^* = \mathbf{B} \mathbf{f}, \quad (54)$$

with $\mathbf{B} \in \mathbb{R}^{3 \times 9}$. For the standard D2Q9 velocity set

$$\mathbf{c}_i \in \{(0, 0), (\pm 1, 0), (0, \pm 1), (\pm 1, \pm 1)\},$$

the explicit entries of \mathbf{B} are listed in Table 2.

Table 2. Explicit form of \mathbf{B} for the D2Q9 lattice, using the Voigt ordering $\mathbf{S}^* = [S_{xx}^*, 2S_{xy}^*, S_{yy}^*]^\top$.

i	0	1	2	3	4	5	6	7	8
(c_{ix}, c_{iy})	(0,0)	(1,0)	(-1,0)	(0,1)	(0,-1)	(1,1)	(-1,1)	(-1,-1)	(1,-1)
$B_{1i} = c_{ix}^2 - c_s^2$	$-c_s^2$	$1 - c_s^2$	$1 - c_s^2$	$-c_s^2$	$-c_s^2$	$1 - c_s^2$	$1 - c_s^2$	$1 - c_s^2$	$1 - c_s^2$
$B_{2i} = 2c_{ix}c_{iy}$	0	0	0	0	0	2	-2	2	-2
$B_{3i} = c_{iy}^2 - c_s^2$	$-c_s^2$	$-c_s^2$	$-c_s^2$	$1 - c_s^2$					

E derivatives of equilibrium distribution

The fourth-order equilibrium distribution f_i^{eq} is defined as:

$$f_i^{\text{eq}} = \rho w_i \left[1 + \frac{c_i \mathbf{u}}{c_s^2} + \frac{(c_i \mathbf{u})^2}{2c_s^4} - \frac{\mathbf{u}^2}{2c_s^2} - \frac{c_i \mathbf{u}^3}{2c_s^4} + \frac{(c_i \mathbf{u})^3}{6c_s^6} + \frac{\mathbf{u}^4}{8c_s^4} - \frac{c_i^2 \mathbf{u}^4}{4c_s^6} + \frac{(c_i \mathbf{u})^4}{24c_s^8} \right] \quad (55)$$

$$= \rho w_i \left[1 + \frac{c_{xi}u_x + c_{yi}u_y}{c_s^2} + \frac{(c_{xi}u_x + c_{yi}u_y)^2}{2c_s^4} - \frac{u_x^2 + u_y^2}{2c_s^2} - \frac{c_{xi}u_x^3 + c_{yi}u_y^3}{2c_s^4} + \frac{(c_{xi}u_x + c_{yi}u_y)^3}{6c_s^6} + \frac{(u_x^2 + u_y^2)^2}{8c_s^4} - \frac{(c_{xi}^2 + c_{yi}^2)(u_x^2 + u_y^2)^2}{4c_s^6} + \frac{(c_{xi}u_x + c_{yi}u_y)^4}{24c_s^8} \right]. \quad (56)$$

and the derivatives are

$$\frac{\partial f_i^{\text{eq}}}{\partial \rho} = w_i \left[1 + \frac{c_{xi}u_x + c_{yi}u_y}{c_s^2} + \frac{(c_{xi}u_x + c_{yi}u_y)^2}{2c_s^4} - \frac{u_x^2 + u_y^2}{2c_s^2} - \frac{c_{xi}u_x^3 + c_{yi}u_y^3}{2c_s^4} + \frac{(c_{xi}u_x + c_{yi}u_y)^3}{6c_s^6} + \frac{(u_x^2 + u_y^2)^2}{8c_s^4} - \frac{(c_{xi}^2 + c_{yi}^2)(u_x^2 + u_y^2)^2}{4c_s^6} + \frac{(c_{xi}u_x + c_{yi}u_y)^4}{24c_s^8} \right] \quad (57)$$

$$\frac{\partial f_i^{\text{eq}}}{\partial u_x} = \rho w_i \left[\frac{c_{xi}}{c_s^2} + \frac{(c_{xi}u_x + c_{yi}u_y)c_{xi}}{c_s^4} - \frac{u_x}{c_s^2} - \frac{3c_{xi}u_x^2}{2c_s^4} + \frac{(c_{xi}u_x + c_{yi}u_y)^2 c_{xi}}{2c_s^6} + \frac{u_x(u_x^2 + u_y^2)}{2c_s^4} - \frac{(c_{xi}^2 + c_{yi}^2)(u_x^2 + u_y^2)u_x}{c_s^6} + \frac{(c_{xi}u_x + c_{yi}u_y)^3 c_{xi}}{6c_s^8} \right] \quad (58)$$

$$\frac{\partial f_i^{\text{eq}}}{\partial u_y} = \rho w_i \left[\frac{c_{yi}}{c_s^2} + \frac{(c_{xi}u_x + c_{yi}u_y)c_{yi}}{c_s^4} - \frac{u_y}{c_s^2} - \frac{3c_{yi}u_y^2}{2c_s^4} + \frac{(c_{xi}u_x + c_{yi}u_y)^2 c_{yi}}{2c_s^6} + \frac{u_y(u_x^2 + u_y^2)}{2c_s^4} - \frac{(c_{xi}^2 + c_{yi}^2)(u_x^2 + u_y^2)u_y}{c_s^6} + \frac{(c_{xi}u_x + c_{yi}u_y)^3 c_{yi}}{6c_s^8} \right] \quad (59)$$